

J. Plasma Phys. (2025), vol. 91, E16 © The Author(s), 2025. Published by Cambridge University Press

This is an Open Access article, distributed under the terms of the Creative Commons Attribution licence (http://creativecommons.org/licenses/by/4.0/), which permits unrestricted re-use, distribution and reproduction, provided the original article is properly cited. doi:10.1017/S0022377824001107

A quasi-linear model of electromagnetic turbulent transport and its application to flux-driven transport predictions for STEP

M. Giacomin ^{101,2},†, D. Dickinson ¹⁰², W. Dorland ^{103,4}, N.R. Mandell ¹⁰⁵, A. Bokshi², F.J. Casson⁶, H.G. Dudding⁶, D. Kennedy ¹⁰⁶, B.S. Patel ¹⁰⁶ and C.M. Roach ¹⁰⁶

¹Dipartimento di Fisica "G. Galilei", Università degli Studi di Padova, Padua, Italy
 ²York Plasma Institute, University of York, York YO10 5DD, UK
 ³Department of Physics, University of Maryland, College Park, MD 20740, USA
 ⁴Institute for Research in Electronics and Applied Physics, University of Maryland, College Park, MD 20742, USA

⁵Princeton Plasma Physics Laboratory, Princeton, NJ 08543, USA
⁶UKAEA (United Kingdom Atomic Energy Authority), Culham Campus, Abingdon, Oxfordshire OX14 3DB, UK

(Received 26 April 2024; revised 10 July 2024; accepted 12 July 2024)

A quasi-linear reduced transport model is developed from a database of high- β electromagnetic nonlinear gyrokinetic simulations performed with spherical tokamak for energy production (STEP) relevant parameters. The quasi-linear model is fully electromagnetic and accounts for the effect of equilibrium flow shear using a novel approach. Its flux predictions are shown to agree quantitatively with predictions from local nonlinear gyrokinetic simulations across a broad range of STEP-relevant local equilibria. This reduced transport model is implemented in the T3D transport solver that is used to perform the first flux-driven simulations for STEP to account for transport from hybrid kinetic ballooning mode turbulence, which dominates over a wide region of the core plasma. Nonlinear gyrokinetic simulations of the final transport steady state from T3D return turbulent fluxes that are consistent with the reduced model, indicating that the quasi-linear model may also be appropriate for describing the transport steady state. Within the assumption considered here, our simulations support the existence of a transport steady state in STEP with a fusion power comparable to that in the burning flat top of the conceptual design, but do not demonstrate how this state can be accessed.

Key words: fusion plasma, plasma confinement, plasma simulation

†Email address for correspondence: maurizio.giacomin@unipd.it

1. Introduction

The design of future tokamaks requires accurate evaluations of the core turbulent transport, which is most reliably modelled using high-fidelity gyrokinetic simulations that have been validated extensively against experiments. However, these simulations are computationally very expensive and, for reasons of computational tractability, reduced turbulent transport models are more routinely used in the design of plasma scenarios. Transport steady-state fusion plasma solutions can be calculated in reasonable times with relatively modest compute resource, using reduced physics-based transport models, such as TGLF (Staebler, Kinsey & Waltz 2005, 2007) and QualiKiz (Bourdelle et al. 2015; Citrin et al. 2017). These models combine a fast and simplified approach to find the linearly dominant eigenmodes (by either solving gyrofluid equations, or using a simplified gyrokinetic solver) together with a saturation rule (Casati et al. 2009; Staebler et al. 2016; Stephens et al. 2021; Dudding et al. 2022). We note, however, that these reduced models of turbulent transport have mainly been validated in electrostatic turbulence regimes (Mariani et al. 2018; Rodriguez-Fernandez et al. 2019; Casson et al. 2020; Luda et al. 2021; Marin et al. 2021; Angioni et al. 2022; Ho et al. 2023) and their application to high- β spherical tokamaks, where electromagnetic turbulence is expected to be important (Kennedy et al. 2023: Giacomin et al. 2024), needs to be carefully assessed (Patel 2021).

Various flat-top operating points of the Spherical Tokamak for Energy Production (STEP) (Wilson et al. 2020; Meyer 2022) have been developed using the integrated modelling suite JINTRAC (Romanelli et al. 2014) and the JETTO transport module with a simple Bohm gyro-Bohm transport modelling tuned to a confinement scaling (Meyer 2022; Tholerus et al. 2024). A gyrokinetic linear analysis of one of the most promising STEP flat-top operating points, STEP-EC-HD (Tholerus et al. 2024), is reported in Kennedy et al. (2023). This reveals dominant microinstabilities at the ion gyroscale, that share many properties of the kinetic ballooning mode (KBM). This dominant mode, labelled hybrid-KBM in Kennedy et al. (2023), is unstable over a wide radial range of the plasma, and connects to ion temperature gradient (ITG) and trapped electron mode (TEM) instabilities at low β . A subsequent nonlinear gyrokinetic investigation, detailed in Giacomin et al. (2024), shows that, if equilibrium flow shear is neglected, turbulent transport from hybrid-KBMs significantly exceeds the available sources at mid-radius in STEP-EC-HD, thus highlighting the importance of accounting for hybrid-KBM turbulence in developing consistent flat-top operating points for STEP. The saturation level of hybrid-KBM turbulence far above threshold is, however, very sensitive to equilibrium flow shear (the sensitivity to flow shear is decreased near threshold, as shown in this work) and, at moderate shearing rates, transport fluxes reduce significantly towards values consistent with the assumed sources in STEP. The work carried out by Giacomin et al. (2024) also shows that the heat flux depends strongly on the parameter $\beta' = \partial \beta / \partial \rho$ (where $\beta = 2\mu_0 p/B^2$, p is the total pressure, B is the magnetic field and ρ is the radial coordinate). As β' is increased above its nominal value, hybrid-KBMs get stabilised and more slowly growing microtearing modes (MTMs), which are more resilient, take over as the dominant modes. On the STEP surface analysed in Giacomin et al. (2024), MTMs drive a significantly lower level of turbulent transport that is more compatible with the assumed sources. A reduced transport model for electromagnetic hybrid-KBM turbulence is clearly required to design flat-top operating points in STEP and to simulate access to them (Mitchell et al. 2023).

High-fidelity tools to evolve plasma equilibrium profiles on the transport time scale have been developed in recent years by coupling transport solvers to local or global gyrokinetic codes. These codes, such as TANGO-GENE (Di Siena *et al.* 2022), PORTALS-CGYRO

(Rodriguez-Fernandez, Howard & Candy 2022) and TRINITY (Barnes et al. 2010), exploit the enormous separation between the time scales associated with turbulence and equilibrium transport, to evolve plasma profiles self-consistently with the turbulence. For instance, PORTALS-CGYRO has been recently applied to perform the first flux-matched nonlinear gyrokinetic predictions of SPARC profiles, where Gaussian process regression techniques have been applied to optimise the transport solver (Rodriguez-Fernandez et al. 2022). Naturally, high-fidelity models require considerably more computational resources than using reduced transport models; and their application to STEP is computationally prohibitively expensive, because each of the many nonlinear local simulations required by a transport solver costs more than 10⁵ core hours. Furthermore, starting from an initial state that strongly violates power balance increases significantly the number of nonlinear gyrokinetic simulations required for profile convergence (power balance is very poorly satisfied at several radial locations in STEP-EC-HD as assumed in scenario design with JINTRAC, which provides the initial condition in our flux-driven transport calculations). There is therefore an increasing interest in developing low-cost and high-fidelity transport solvers that can be exploited in integrated modelling, such as the fast and accurate turbulent transport model recently developed by Citrin et al. (2023), where the saturation rule, calibrated to a set of nonlinear GENE simulations, is combined with a neural network regression to perform flux-matched predictions of the ITER baseline scenario.

In this work, we develop a quasi-linear reduced transport model from a database of nonlinear local gyrokinetic simulations of hybrid-KBM turbulence for a range of STEP local equilibria. The reduced transport model is based on a quasi-linear metric that combines a saturation rule and quasi-linear flux weights evaluated from linear gyrokinetic calculations. The functional dependence of the heat flux on this quasi-linear metric is developed from a fit to the database of nonlinear simulations. This reduced transport model is implemented in T3D (or Trinity3D) (Qian *et al.* 2022), a new Python version of TRINITY (Barnes *et al.* 2010) which is used in this paper to perform the first flux-driven simulations to model transport from hybrid-KBM turbulence in STEP.

The paper is organised as follows. Section 2 presents a brief overview of linear and nonlinear simulations from various radial locations in a STEP flat-top operating point. The reduced turbulent transport model, obtained from a fit to the nonlinear gyrokinetic database, is presented in § 3. Section 4 describes the implementation of the reduced model in T3D and its exploitation for the first predictive transport simulations to model hybrid-KBM turbulence in STEP. The robustness of the reduced model is assessed in § 5, by comparing the reduced model transport fluxes against a new set of nonlinear gyrokinetic simulations for different surfaces of the new T3D transport steady state. Finally the main conclusions are presented in § 6.

2. Overview of STEP local gyrokinetic simulations

This section gives a brief overview of the linear and nonlinear gyrokinetic analysis of the STEP-EC-HD flat-top operating point reported in Kennedy *et al.* (2023) and Giacomin *et al.* (2024), and motivates the need for a new reduced model of transport from electromagnetic turbulence in STEP-like regimes.

Table 1 gives local equilibrium parameters from six radial surfaces (with low-order rational values of the safety factor q) in STEP-EC-HD (Meyer 2022; Tholerus *et al.* 2024)²:

¹This is true even when Gaussian process regression techniques are used to reduce the number of solver iterations (Rodriguez-Fernandez *et al.* 2022).

²This STEP-EC-HD equilibrium is at SimDB UUID:2bb77572-d832-11ec-b2e3-679f5f37cafe, alias: smars/jetto/step/88888/apr2922/seq-1. Local quantities were obtained from the global STEP-EC-HD equilibrium using the pyrokinetics Python library (Patel *et al.* 2024).

Local parameters of STEP-EC-HD							
Ψ_n	0.15	0.36	0.49	0.58	0.71	0.80	
q	2.5	3.0	3.5	4.0	5.0	6.0	
$rac{q}{\hat{s}}$	0.3	0.6	1.2	1.6	2.2	3.2	
ho	0.34	0.54	0.64	0.70	0.80	0.85	
κ'	-0.09	-0.09	0.06	0.19	0.49	0.63	
δ	0.16	0.23	0.29	0.32	0.40	0.45	
δ'	0.44	0.36	0.46	0.54	0.70	1.05	
Δ'	-0.23	-0.34	-0.40	-0.44	-0.49	-0.53	
eta_e	0.17	0.12	0.09	0.07	0.05	0.03	
eta'	-0.38	-0.45	-0.48	-0.47	-0.44	-0.40	
$ ho_*$	0.0033	0.0028	0.0026	0.0024	0.0022	0.0020	
a/L_{n_e}	0.09	0.45	1.06	1.54	2.58	3.43	
a/L_{T_e}	0.92	1.32	1.58	1.77	2.15	2.58	
a/L_{n_D}	0.09	0.45	1.06	1.54	2.58	3.43	
a/L_{T_D}	1.19	1.67	1.82	1.96	2.41	3.28	
$n_e (10^{20} \text{ m}^{-3})$	2.0	1.9	1.8	1.7	1.4	1.2	
$T_e (\text{keV})$	15.6	11.8	10.3	9.2	7.7	6.8	
$T_D ext{ (keV)}$	17.8	12.5	10.6	9.4	7.7	6.8	
Area (m ²)	217	319	362	389	435	456	
$Q_{\rm JETTO}~({ m MW~m^{-2}})$	0.8	0.9	0.8	0.7	0.6	0.5	
$\Gamma_{\text{JETTO}} (10^{20} \text{ m}^{-2} \text{ s}^{-1})$	0.01	0.06	0.11	0.16	0.21	0.22	

TABLE 1. Local parameters on low-order rational surfaces of STEP-EC-HD. The deuterium and tritium densities are equal to half the electron density. The deuterium and tritium temperatures are equal. All parameters are defined in the main text.

 Ψ_n represents the normalised poloidal magnetic flux; q the safety factor; \hat{s} the magnetic shear; ρ is a normalised flux label (half the flux-surface mid-plane diameter normalised to the minor radius a); κ and κ' the elongation and its radial derivative; δ and δ' the triangularity and its radial derivative; and Δ' the radial derivative of the Shafranov shift; local value of $\beta_e = 2\mu_0 p_e/B_0^2$, and its radial derivative β' ; $\rho_* = \rho_s/a$ where $\rho_s = c_s/\Omega_D$ is the local ion sound Larmor radius, with $c_s = \sqrt{T_e/m_D}$, $\Omega_D = eB_0/m_D$, T_e the local electron temperature, m_D the deuterium mass and B_0 the toroidal magnetic field at the central major radius on the surface; the normalised logarithmic radial derivatives of the electron and deuterium density, $a/L_{n_s} \equiv (1/n_s)\partial n_s/\partial \rho$, and temperature, $a/L_{T_s} \equiv (1/T_s)\partial T_s/\partial \rho$; n_e the value of the electron density (the deuterium and tritium densities are equal, i.e. $n_D = n_T = n_e/2$); T_e and T_D the electron and deuterium temperature (the tritium and deuterium temperatures are equal); and the target values of the heat and particle flux computed in JETTO from the expected heat and particle sources of STEP-EC-HD.

2.1. Linear simulation results

Faithfully capturing the linear physics will be critical to the quasi-linear model, so here we briefly revisit the linear analysis of STEP-EC-HD, detailed in Kennedy *et al.* (2023). Linear local gyrokinetic simulations were carried out on six radial surfaces using the GS2 code (Dorland *et al.* 2000; Barnes *et al.* 2022). These calculations included three plasma species (electron, deuterium and tritium) and used the following numerical resolutions: extended parallel domain in ballooning angle spanning $-7\pi < \theta < 7\pi$ ($n_{period} = 4$), 65 parallel grid points in each $[-\pi, \pi]$ interval ($n_{\theta} = 65$), 40 pitch angles ($n_{\lambda} = 40$) and

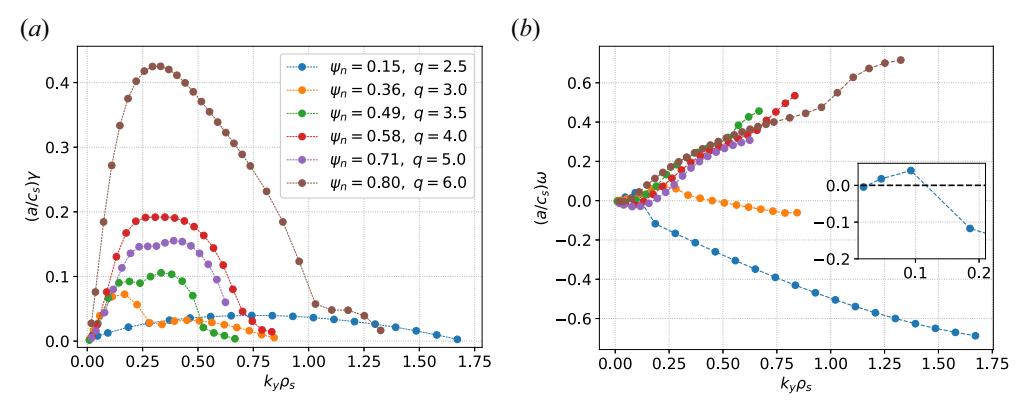


FIGURE 1. Growth rate (a) and mode frequency (b) as functions of the binormal wave vector k_y at various radial surfaces of STEP-EC-HD. The inset in (b) shows the transition to positive frequency values at low k_y of $\Psi_n = 0.15$.

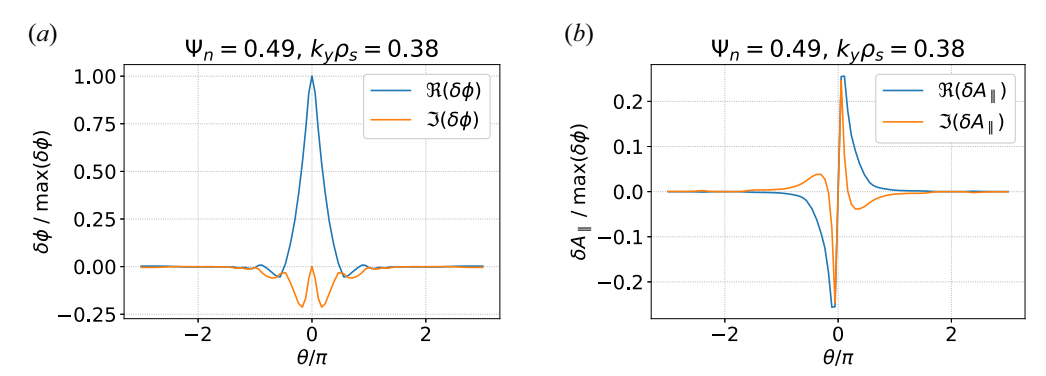


FIGURE 2. Parallel mode structure of $\delta\phi$ (a) and δA_{\parallel} (b) both normalised to max($\delta\phi$) for the most unstable mode with $k_{\nu}\rho_{s}\simeq0.4$. Figure adapted from Kennedy *et al.* (2023).

12 energy grid points ($n_{\epsilon}=12$). The extended ballooning domain is increased to $n_{\rm period}=32$ on the innermost surface at $\Psi_n=0.15$ in order to resolve more extended MTMs found on this surface. All calculations are fully electromagnetic, including $\delta\phi$, δA_{\parallel} and δB_{\parallel} , and were carried at $\theta_0=0$ unless otherwise specified.

Figure 1 shows the growth rate and the mode frequency as functions of the binormal wave vector $k_y \rho_s$ on the six surfaces. No unstable modes are found at $k_y \rho_s > 1.8$ on any of the surfaces considered here. The maximum normalised local growth rate generally increases from the innermost to the outermost radial surface, and a sign change in the dominant mode frequency from mostly negative across most of the spectrum at $\Psi_n = 0.15$ to mostly positive at $\Psi_n = 0.36$, clearly indicates an instability transition going outwards from the core.

The dominant mode at $\Psi_n=0.49$ has been labelled as a hybrid-KBM because it shares many properties with KBM and exhibits ITG and TEM contributions to the linear drive (Kennedy *et al.* 2023). Figure 2 shows the parallel mode structure of $\delta \phi$ and δA_{\parallel} of the dominant hybrid-KBM at $k_v \rho_s \simeq 0.4$ on $\Psi_n=0.49$.

³See Kennedy *et al.* (2024) for a detailed discussion on the importance of δB_{\parallel} in STEP.

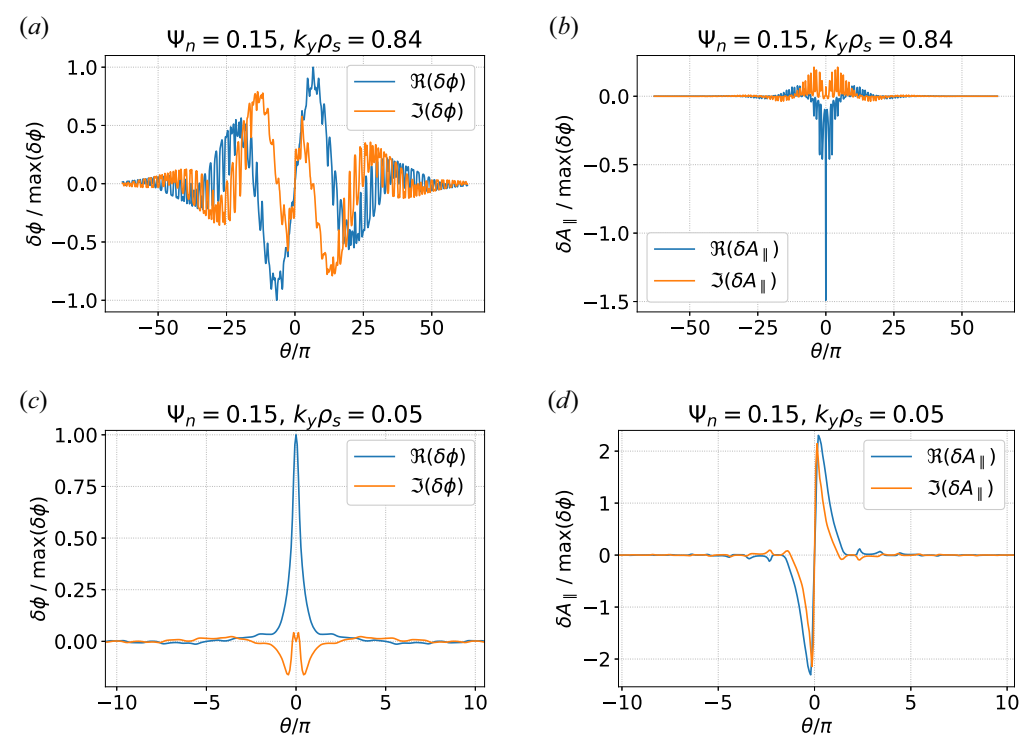


FIGURE 3. Parallel mode structure of $\delta\phi$ (a,c) and δA_{\parallel} (b,d) both normalised to max($\delta\phi$) for the unstable mode with $k_{y}\rho_{s}\simeq0.84$ (a,b) and $k_{y}\rho_{s}\simeq0.05$ (c,d) at $\Psi_{n}=0.15$.

On the innermost surface at $\Psi_n=0.15$, however, the dominant modes have negative frequency and very different parallel mode structures. These are illustrated in figures 3(a) and 3(b) for the fastest growing mode at $k_y \rho_s \simeq 0.84$: $\delta \phi$ has odd parity and is highly extended in θ whilst δA_{\parallel} is very localised at $\theta=0$ with even parity. Amplitudes of $e\delta \phi/T_e$ and $\delta A_{\parallel}/(\rho_s B_0)$ are comparable, indicating that the mode is strongly electromagnetic. These negative frequency modes propagate in the electron diamagnetic drift direction, and have the typical properties expected of MTMs (Applegate *et al.* 2004). On the same surface at the lowest k_y , on the other hand, the dominant mode switches to a positive frequency (see the inset in figure 1b) and very different parallel mode structures in $\delta \phi$ and δA_{\parallel} . The parallel mode structure of a low k_y mode with positive frequency is shown in figures 3(c) and 3(d): the parallel structure closely resemble figure 2, indicating that the hybrid-KBM is linearly dominant at low k_y . Although these low k_y hybrid-KBMs are only weakly unstable, they nevertheless contribute significantly to the turbulent transport, as will be discussed in § 2.2.

The analysis of Kennedy *et al.* (2023) showed that hybrid-KBM is highly ballooned with growth rates that are extremely sensitive of the ballooning parameter, θ_0 . This suggests that hybrid-KBM turbulence should be sensitive to equilibrium flow shear, as was subsequently confirmed in Giacomin *et al.* (2024). Figure 4(*b*) shows the dependence on θ_0 of growth rates on the outermost surface at $\Psi_n = 0.8$, where hybrid-KBMs similar to the modes at $\Psi_n = 0.49$ dominate: the hybrid-KBM growth rates are strongly suppressed as θ_0 increases from zero (the slowly growing unstable mode on this surface at $\theta_0 = \pi$ and $k_y \rho_s \simeq 0.03$ is a MTM). Figure 4(*a*), however, shows that the situation is quite different on the innermost surface at $\Psi_n = 0.15$: here, the MTM growth rates at $k_y \rho_s \simeq 0.8$ and $k_y \rho_s \simeq 1.3$ are

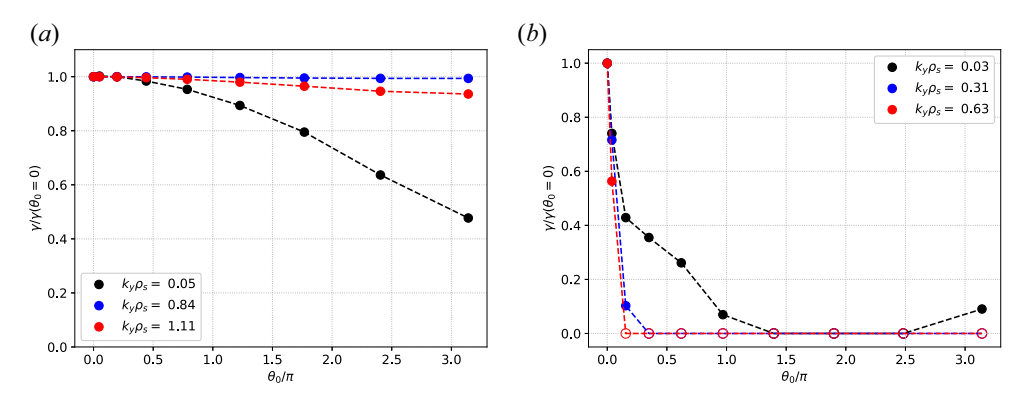


FIGURE 4. Dependence of the growth rate on θ_0 at three different values of $k_y \rho_s$ on the surfaces at $\Psi_n = 0.15$ (a) and $\Psi_n = 0.8$ (b). Stable modes are shown with $\gamma = 0$ and open markers.

Ψ_n	$\Delta k_y \rho_s$	$k_{y,\max}\rho_s$	$\Delta k_{x} \rho_{s}$	$k_{x,\max}\rho_s$	$n_{ heta}$	n_{μ}	n_v
0.15	0.02	1.28	0.02	2.56	32	16	32
0.36	0.016	1.02	0.03	0.96	32	16	32
0.8	0.02	1.28	0.025	1.6	32	16	32

Table 2. Numerical resolution of the nonlinear GENE simulations at the different radial locations. In the table, n_{μ} is number of grid points in the $\mu = v_{\perp}^2/(2B)$ direction and n_v is number of velocity grid points.

insensitive to θ_0 , although in contrast the dominant hybrid-KBM at $k_y \rho_s \simeq 0.05$ has a growth rate that decreases with θ_0 , albeit remaining unstable across the entire θ_0 domain.

2.2. Nonlinear simulations results

This section presents a brief overview of local nonlinear gyrokinetic simulations carried out on three radial surfaces, $\Psi_n \in \{0.15, 0.36, 0.8\}$, of STEP-EC-HD. This analysis extends the investigation carried out at $\Psi_n = 0.49$ by Giacomin *et al.* (2024), providing further nonlinear simulations to be used in the development of a reduced turbulent transport model to account for hybrid-KBMs. The nonlinear gyrokinetic simulations are carried out with the GENE code (Jenko *et al.* 2000) using the advanced Sugama collision operator (Sugama, Watanabe & Nunami 2009). The numerical resolutions used in these simulations is reported in table 2. We highlight the higher radial resolution required by MTMs at $\Psi_n = 0.15$. Simulations are performed without and with equilibrium flow shear. All the simulations are performed over a time interval that covers at least a growth time of the slowest growing low k_y mode of each surface, corresponding to several growth times of the most unstable mode.

2.2.1. Innermost surface dominated linearly by MTMs ($\Psi_n = 0.15$)

Figure 5 shows the time trace of the total heat and particle flux k_y spectrum, normalised to $Q_{\rm gB} = \rho_*^2 n_e T_e c_s$ and $\Gamma_{\rm gB} = \rho_*^2 n_e c_s$, from a nonlinear simulation at $\Psi_n = 0.15$ without

⁴See Hardman *et al.* (2023) and Patel *et al.* (2023) for a detailed discussion of the relationship between $\gamma^{\text{MTM}}(\theta_0)$ and the sensitivity of MTM turbulence to equilibrium flow shear.

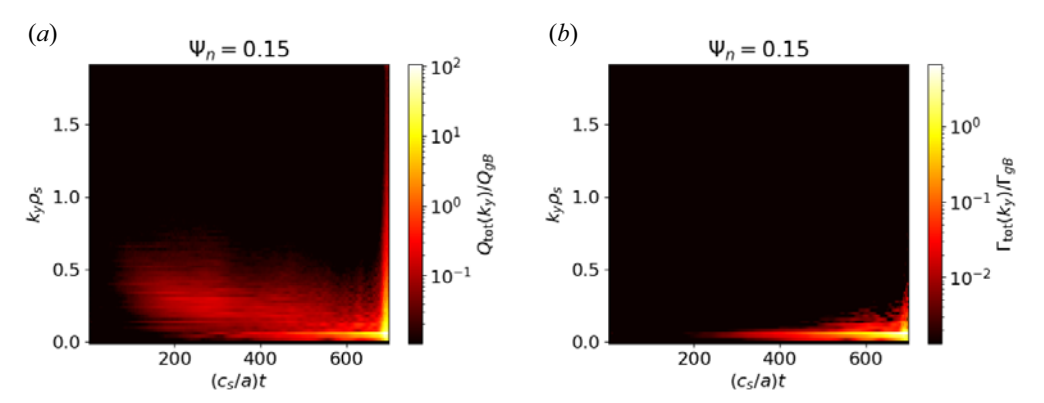


FIGURE 5. Total heat (a) and particle (b) flux as functions of k_y and time from the nonlinear simulation at $\Psi_n = 0.15$. The equilibrium flow shear is not included.

equilibrium flow shear. The heat flux contribution from $k_y \rho_s \sim 0.25$ increases until $t \simeq 250 \, a/c_s$ where it reaches values of the order of $Q_{\rm gB}$, and then remains approximately constant until $t \simeq 600 \, a/c_s$. The particle flux contributions from $k_y \rho_s > 0.2$ are negligible, as expected from MTM-driven turbulent transport in this k_y range on this surface (see, e.g. Doerk *et al.* (2011), Guttenfelder *et al.* (2011), Hatch *et al.* (2016) and Giacomin *et al.* (2023) for details on MTM turbulence). On the other hand, the heat and particle flux contributions from $k_y \rho_s < 0.2$ steadily grow (the total heat flux grows to exceed 100 $Q_{\rm gB}$) and show no signs of saturation within the simulated time interval. Figure 5 suggests that the large turbulent fluxes at low k_y are driven by the hybrid-KBMs that are linearly unstable at the lowest binormal wavenumbers in figure 1.

The sensitivity of $\gamma^{\text{KBM}}(k_y \rho_s = 0.05)$ to θ_0 shown in figure 4(a), together with the low hybrid-KBM growth rate, implies that equilibrium flow shear may be important here even at small shearing rates near the diamagnetic level, γ_E^{dia} , where

$$\gamma_E^{\text{dia}} = \frac{\rho}{q} \frac{d}{\rho} \left(\frac{E_r}{RB_{\theta}} \right) = \frac{\rho}{q} \frac{d}{\rho} \left[\frac{1}{RB_{\theta}} \left(\frac{1}{n_i e} \frac{dp_i}{dr} + v_{\phi} B_{\theta} - v_{\theta} B_{\phi} \right) \right], \tag{2.1}$$

with E_r the neoclassical radial electric field, n_i and p_i the thermal ion density and pressure, v_θ and v_ϕ the poloidal and toroidal velocities and B_θ and B_ϕ the poloidal and toroidal magnetic field components. In the JINTRAC flat-top operating point considered here, v_θ is evaluated using NCLASS (Houlberg *et al.* 1997) while $v_\phi = 0$. Figure 6 shows the time trace of the electrostatic and electromagnetic heat and particle fluxes from a nonlinear simulation at $\Psi_n = 0.15$ with $\gamma_E = \gamma_E^{\rm dia} \simeq 0.01 \, c_s/a$. When the equilibrium flow shear is included at $t = 150 \, a/c_s$, the heat flux reduces slightly and saturates at approximately 5 MW m⁻². The runaway fluxes are completely avoided in the simulation with $\gamma_E = 0.01 \, c_s/a$. Figure 7 shows, however, that, even with this level of flow shear, the saturated heat and particle fluxes nevertheless remain above the values required to achieve a transport steady state on this surface in STEP-EC-HD with the available heat and particle sources.

2.2.2. Further out radially where hybrid-KBMs dominate ($\Psi_n = 0.36$)

Figure 8 compares the heat and particle fluxes averaged over time in the saturated phase from nonlinear simulations without and with equilibrium flow shear of the order of the diamagnetic level, $\gamma_E^{\rm dia} \approx 0.05 \, c_s/a$. Although this nonlinear simulation at $\gamma_E = 0$ appears to saturate within the time simulated, the corresponding heat and particle fluxes exceed

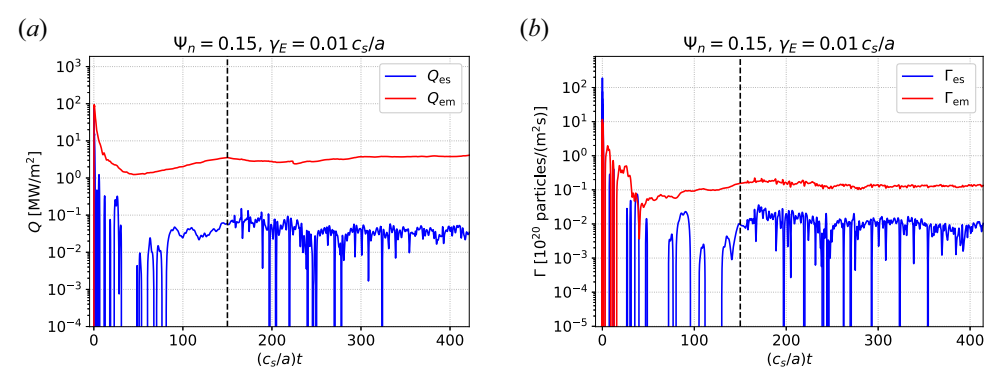


FIGURE 6. Time trace of the electromagnetic and electrostatic heat (a) and particle (b) fluxes from the nonlinear simulation at $\Psi_n = 0.15$ with $\gamma_E = 0.01 c_s/a$. The equilibrium flow shear is active from $t = 150 a/c_s$, as indicated by the dashed vertical line.

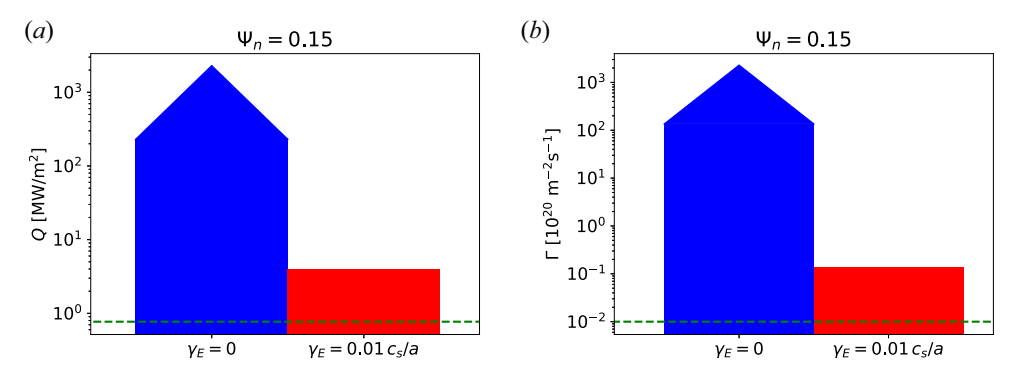


FIGURE 7. Total heat (a) and particle (b) fluxes from nonlinear simulations at $\Psi_n = 0.15$ with (red) and without (blue) equilibrium flow shear. The heat and particle fluxes in the simulation without equilibrium flow shear exceed the value of 10^2 MW m⁻² and 10^{22} particles (m² s)⁻¹ with no saturation within the simulation time considered here, as indicated by the triangle on the top of the bar. The dashed horizontal line denotes the target heat and particle flux values at $\Psi_n = 0.15$ computed from the JETTO heat and particle sources.

STEP-EC-HD transport steady-state values for this surface by more than three orders of magnitude. When flow shear is included, both heat and particle fluxes reduce significantly, but remain well above the transport steady-state values, as shown in figure 8.

The outermost flux surface, where hybrid-KBMs also dominate ($\Psi_n = 0.8$):

Nonlinear simulations deliver similar findings at $\Psi_n = 0.8$. Figure 9 shows the heat and particle fluxes from nonlinear simulations without and with equilibrium flow shear $(\gamma_E = 0.1 \, c_s/a)$. The simulation without equilibrium flow shear does not saturate within the considered simulation time interval, reaching values larger than 10^3 MW m⁻². The simulation with equilibrium flow shear saturates at much lower values, but turbulent fluxes remain an order of magnitude larger than the transport steady-state values for STEP-EC-HD at $\Psi_n = 0.8$.

2.2.3. *Summary of § 2*

This brief nonlinear survey suggests that anomalous transport would be dominated by hybrid-KBM turbulence across a wide radial region in STEP-EC-HD. In the absence of

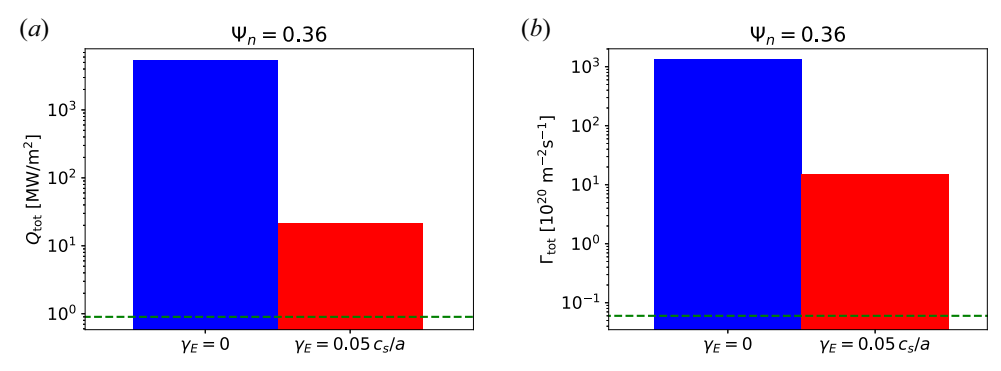


FIGURE 8. Total heat (a) and particle (b) fluxes from nonlinear simulations at $\Psi_n = 0.36$ with (red) and without (blue) equilibrium flow shear. The dashed horizontal line denotes the target flux value at $\Psi_n = 0.36$ computed from JETTO heat and particle sources.

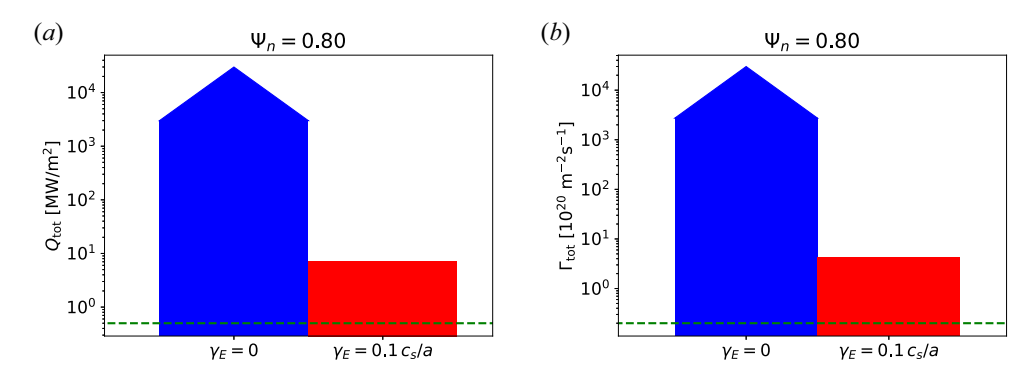


FIGURE 9. Saturated value of the total heat (a) and particle (b) fluxes from nonlinear simulations at $\Psi_n=0.80$ with (red) and without (blue) equilibrium flow shear. The heat and particle fluxes in the simulation without equilibrium flow shear exceed 10^3 MW m⁻² and 10^{23} particles (m² s)⁻¹ with no saturation within the simulation time considered here, as indicated by the triangular arrow at the top of the bar. The dashed horizontal line denotes the target flux value at $\Psi_n=0.80$ computed from the JETTO heat and particle sources.

equilibrium flow shear, the associated turbulent fluxes exceed values required to reach a transport steady state in STEP-EC-HD by several orders of magnitude. The fluxes are very sensitive to flow shear, and including a diamagnetic level of γ_E reduces the fluxes significantly. Nevertheless this is insufficient to reduce fluxes to the values required in a transport steady state; i.e. STEP-EC-HD is not a transport steady state. To reach such a kinetic equilibrium, the temperature and density profiles need to be evolved self-consistently with turbulent transport from hybrid-KBMs. This clearly motivates the need for a computationally affordable reduced model to describe turbulent transport in STEP-relevant regimes. The development of such a model is detailed in the next section.

3. A reduced transport model for STEP

Transport will play an important role in governing all aspects of the plasma scenarios that are viable in STEP, including the fusion power that can be achieved in the flat top. One of the most urgent priorities for the STEP programme is to develop robust physics-based models to predict plasma confinement. The highest-fidelity approach available would use

nonlinear gyrokinetic simulations to compute the turbulent transport, but in STEP-like regimes this is prohibitively expensive computationally even using local gyrokinetics codes. A reduced core transport model is urgently required to describe turbulent transport in high- β STEP regimes faithfully and in a computationally affordable way.

Here, we describe in detail one approach to obtain such a reduced turbulent transport model, retaining first-principles linear physics from gyrokinetic calculations, and exploiting a set of nonlinear gyrokinetic simulations in STEP-relevant regimes to obtain an empirical functional relationship between the quasi-linear and the nonlinear fluxes. We stress that this model is not intended for application beyond STEP plasma conditions, although the general approach may have value for reduced model development in broader plasma regimes. Our approach has some parallel with earlier efforts to improve reduced model descriptions of magnetic flutter transport, where the goal was to better describe transport from KBMs in JET discharges (see Kumar *et al.* 2021).

In local δf gyrokinetics, where the distribution function f is the sum of the equilibrium distribution function f_0 and a perturbation δf , the nonlinear electrostatic $E \times B$ drift term competes with the linear drive, i.e. $\gamma \delta f \sim (k_y \delta \phi/B) k_x \delta f$, at sufficient perturbation amplitude when $\delta \phi/B \sim \gamma/(k_x k_y)$. Quasi-linear models assume saturation occurs when $\partial_x p \sim k_x \delta p$, allowing the total electrostatic heat flux to be estimated as $Q^{\text{ES}} \sim \delta p k_y \delta \phi/B \sim (\gamma/k_x^2) \partial_x p$. If the turbulence is isotropic, with $k_x \sim k_y \sim k_\perp$, this can be written as $Q^{\text{ES}} \sim (\gamma/k_\perp^2) \partial_x p$, corresponding to a turbulent thermal diffusivity of γ/k_\perp^2 .

3.1. Quasi-linear reduced transport model

In the quasi-linear inspired reduced model developed here, the saturation rule describes the total heat flux,⁵ which is modelled as⁶

$$Q_{\rm ql} = Q_0 \Lambda^{\alpha},\tag{3.1}$$

where the quasi-linear metric Λ (involving γ/k_{\perp}^2 , all fields and describing flow shear) is at the heart of the model, and Q_0 and α are constants chosen to fit the total turbulent heat transport in the regime of interest. In § 3.2, Q_0 and α will be optimised to describe the total heat flux from hybrid-KBM turbulence in STEP. Firstly we define Λ and then we specify the species decomposition of the model transport fluxes.

In ballooning space local perturbed modes are labelled by the bi-normal perpendicular wavenumber and ballooning parameter, k_y and θ_0 , respectively. For each mode (i.e. k_y and θ_0) and field $\chi_i \in \{e\delta\phi/T_e, \delta A_{\parallel}/(\rho_s B_0), \delta B_{\parallel}/B_0\}$, we define a perpendicular wavenumber averaged in poloidal angle θ , following Jenko, Dannert & Angioni (2005), as

$$\langle k_{\perp}^2 \rangle_{k_y,\theta_0,i} = \frac{\int d\theta \, k_{\perp}^2(\theta, k_y, \theta_0) J(\theta) \, |\chi_i(\theta)|^2}{\int d\theta \, J(\theta) |\chi_i(\theta)|^2},\tag{3.2}$$

⁵Imposing a saturation rule for the total heat flux implies saturation levels for all the fields, because these are related through the quasi-linear weights; this differs from quasi-linear models where the saturation rule is applied directly to the electrostatic potential, but is similar to the concept of turbulence intensity used to define saturation in some models (Kinsey, Staebler & Waltz 2008).

⁶Note that the relationship between the total heat flux and γ/k_{\perp}^2 depends on the turbulent regime and might not be linear (see e.g. Ricci, Rogers & Dorland 2006; Giacomin & Ricci 2020; Dudding *et al.* 2022). For example, if $\delta p \sim (q\delta\phi/T)p$, the electrostatic heat flux becomes $Q^{\rm ES} \sim (\gamma^2/k_{\perp}^4)(qB/T)k_{\perp}p$. Including the parameter α in (3.1) allows the model to describe such a different turbulence regime.

where $k_{\perp}^2(\theta, k_y, \theta_0) = g^{yy}(\theta)k_y^2 + 2g^{xy}(\theta)k_xk_y + g^{xx}(\theta)k_x^2$, $k_x = \hat{s}\theta_0k_y$, g^{yy} , g^{xx} and g^{xy} are metric tensor elements and $J(\theta)$ is the Jacobian (these geometric quantities are defined for GS2 in Kotschenreuther, Rewoldt & Tang 1995; Dorland *et al.* 2000).

By using $\langle k_{\perp}^2 \rangle_{k_y,\theta_0,i}$ from (3.2) and summing over all three fields, we define

$$\hat{\Lambda}(k_{y}, \theta_{0}) = \sum_{i=1}^{3} \frac{\max_{\theta} |\chi_{i}(k_{y}, \theta_{0}, \theta)|}{\max_{\theta} |\chi_{1}(k_{y}, \theta_{0}, \theta)|} \frac{\gamma(k_{y}, \theta_{0})}{\langle k_{\perp}^{2}(k_{y}, \theta_{0}, \theta)\rangle_{\theta, i}}.$$
(3.3)

When modes are strongly electromagnetic, $\hat{A}(k_y, \theta_0)$ has substantial contributions from magnetic perturbations.⁷ On the other hand, when δA_{\parallel} and δB_{\parallel} vanish (e.g. at low β), (3.3) reduces to the electrostatic model of Jenko *et al.* (2005).

The dependence of $\hat{\Lambda}$ on θ_0 in (3.3) can be exploited to capture the effect of equilibrium flow shear⁸ on the quasi-linear turbulent transport. Equilibrium flow shear advects local modes in the ballooning parameter at a rate $d\theta_0/dt = \gamma_E/\hat{s}$, which is accounted for by averaging $\hat{\Lambda}(k_v, \theta_0)$ over a suitable θ_0 interval

$$\bar{\Lambda}(k_y) = \frac{1}{\theta_{0,\max}(k_y, \gamma_E)} \int_0^{\theta_{0,\max}(k_y, \gamma_E)} \hat{\Lambda}(k_y, \theta_0) d\theta_0, \tag{3.4}$$

where

$$\theta_{0,\text{max}} = \min\left(\frac{\gamma_E}{\hat{s}\gamma}, \pi\right).$$
 (3.5)

The θ_0 interval is the advection range over one growth time, from the typically most unstable mode at $\theta_0 = 0$ to $\theta_{0,\max} = \gamma_E/(\hat{s}\gamma)$, with γ the growth rate at $\theta_0 = 0$. In the low flow shear limit, $\gamma_E \ll \hat{s}\gamma$, $\bar{\Lambda}(k_y)$ reduces to $\hat{\Lambda}(k_y,0)$; in the high flow shear limit where $\gamma_E > \hat{s}\gamma \pi$, the average is calculated over a reduced θ_0 range $[0,\pi]$, justified by periodicity. The θ_0 average in (3.4) allows the quasi-linear model to capture flow shear suppression of turbulence at finite γ_E . We note that, if $\gamma(\theta_0)$ is narrowly peaked close to $\theta_0 = 0$, $\bar{\Lambda}(k_y)$ can be sharply reduced even at small values of γ_E . As shown in figure 4 and in Kennedy *et al.* (2023), the growth rate of hybrid-KBMs can peak strongly at $\theta_0 = 0$ in STEP.

The quasi-linear metric Λ in (3.1) is then obtained by integrating $\bar{\Lambda}(k_y)$ in (3.4) over k_y , and normalised to ρ_*c_s

$$\Lambda = \frac{1}{\rho_* c_s} \int dk_y \, \bar{\Lambda}(k_y)$$

$$= \frac{1}{\rho_* c_s} \int dk_y \frac{1}{\theta_{0,\text{max}}} \int_0^{\theta_{0,\text{max}}} d\theta_0 \sum_{i=1}^3 \frac{\max_{\theta} |\chi_i(k_y, \theta_0, \theta)|}{\max_{\theta} |\chi_1(k_y, \theta_0, \theta)|} \frac{\gamma(k_y, \theta_0)}{\langle k_{\perp}^2(k_y, \theta_0, \theta) \rangle_{\theta, i}}.$$
(3.6)

This quantity depends only on linear physics, so its evaluation requires only linear gyrokinetic simulations over the unstable spectrum in (k_y, θ_0) . We highlight that Λ has been derived rather generally without any specific assumption on the turbulence regime. The parameters Q_0 and α , which appear in (3.1), are the only free parameters to influence the turbulence saturation level in this reduced model.

⁷The quantity $\hat{\Lambda}(k_y, \theta_0)$ defined in (3.3) is implemented in GS2 and available as an output from commit 415983d.

⁸A similar novel approach to flow shear has recently been included in a new quasi-linear model for momentum transport (Sun *et al.* 2024).

Species heat and particle fluxes are obtained (from (3.7) and (3.8) below) using the total model heat flux, $Q_{ql} = Q_0 \Lambda^{\alpha}$ defined in (3.1) that sets the turbulence saturation amplitude, together with the quasi-linear weights $Q_{l,s}/Q_l$ and $\Gamma_{l,s}/Q_l$, where $Q_{l,s}$ and $\Gamma_{l,s}$ are the linear heat and particle fluxes for species s, and $Q_l = \sum_s Q_{l,s}$ is the total linear heat flux; all linear fluxes are taken from the final time point in a converged linear simulation for a given mode (i.e. k_y , θ_0). The quasi-linear weights apportion contributions to transport fluxes for each species for a given mode (depending on k_y and θ_0) must be included in the integrands of (3.7) and (3.8) to obtain the total species heat and particle fluxes

$$Q_{\text{ql},s} = Q_0 \Lambda^{\alpha - 1} \left(\frac{1}{\rho_* c_s} \right) \int dk_y \, \frac{1}{\theta_{0,\text{max}}} \int_0^{\theta_{0,\text{max}}} d\theta_0 \, \frac{Q_{l,s}(k_y, \theta_0)}{Q_l(k_y, \theta_0)} \hat{A}(k_y, \theta_0)$$
(3.7)

$$\Gamma_{\text{ql},s} = Q_0 \Lambda^{\alpha - 1} \left(\frac{1}{\rho_* c_s} \right) \int dk_y \, \frac{1}{\theta_{0,\text{max}}} \int_0^{\theta_{0,\text{max}}} d\theta_0 \, \frac{\Gamma_{\text{l},s}(k_y, \, \theta_0)}{Q_1(k_y, \, \theta_0)} \, \hat{\Lambda}(k_y, \, \theta_0), \tag{3.8}$$

where we note that $\sum_{s} Q_{ql,s} = Q_{ql} = Q_0 \Lambda^{\alpha}$.

3.2. Application to STEP-relevant regimes

The parameters Q_0 and α , which link Λ to the quasi-linear heat flux $Q_{\rm ql}$ via (3.1), are tuned here to optimise the description of the total heat transport from hybrid-KBM turbulence in STEP. Suitable values are determined by fitting the nonlinear saturated heat fluxes from a set of nonlinear gyrokinetic simulations for STEP-relevant local equilibria. This database contains nonlinear simulations performed using local parameters from various reference surfaces in STEP-EC-HD. The parameter scans reported in Kennedy *et al.* (2023) and Giacomin *et al.* (2024) already cover many of the most important local parameters, including pressure gradient, β , flow shear, q and \hat{s} , to which hybrid-KBM turbulence is sensitive. Those scans provide the bulk of the database used to develop the quasi-linear model. In detail, we include several parameter scans at $\Psi_n = 0.49$ with $\gamma_E \in \{0.05, 0.1, 0.2\}$ c_s/a , $q \in \{3, 3.5, 4.0, 4.5\}$, $\beta \in \{0.005, 0.02, 0.09\}$ and $L_{p,ref}/L_p \in \{0.8, 1.0, 1.2\}$ from Giacomin *et al.* (2024) and an additional scan with $\hat{s} \in \{0.3, 0.6, 1.2\}$ for $\gamma_E = 0$. The database also includes the simulations at $\Psi_n = 0.36$ ($\gamma_E = 0$ and $\gamma_E = 0.05$ c_s/a) and at $\gamma_E = 0.8$ ($\gamma_E = 0.1$ $\gamma_E = 0.8$) are $\gamma_E = 0.8$ ($\gamma_E = 0.8$) are $\gamma_E = 0.8$). So, $\gamma_E = 0.8$ ($\gamma_E = 0.8$) are $\gamma_E = 0.8$ ($\gamma_E = 0.8$) are $\gamma_E = 0.8$) are $\gamma_E = 0.8$.

Figure 10 compares the total normalised heat flux, $Q/Q_{\rm gB}$, from nonlinear simulations with that from the best-fit quasi-linear model defined in (3.1), as functions of Λ , where Λ is defined in (3.6) and obtained from linear gyrokinetic simulations. Each point in figure 10 corresponds to a nonlinear simulation and the colour distinguishes simulations with and without equilibrium flow shear. The uncertainty in the average nonlinear heat flux from each simulation is taken as the standard deviation in the saturated phase. These uncertainties are accounted for by using a weighted fit to obtain the best values for the model parameters Q_0 and α . This gives $Q_0/Q_{\rm gB} \simeq 25$ and $\alpha \simeq 2.5$, with a fitting quality of $R^2 \simeq 0.8$. The unweighted fit returns values of α and Q_0 that differ approximately by 20%, which can be considered as an estimate of the uncertainty in the fit values. The quasi-linear model reproduces acceptably well the nonlinear heat flux across a range of more than three orders of magnitude, although we highlight significant scatter. The discrepancy between the reduced model and simulations approaches an order of magnitude in a few cases, illustrating a limitation in the reduced transport model. A comparison of the nonlinear

⁹The stationary phases are identified by applying the augmented Dickey–Fuller test to the flux time traces, as described in Giacomin *et al.* (2024).

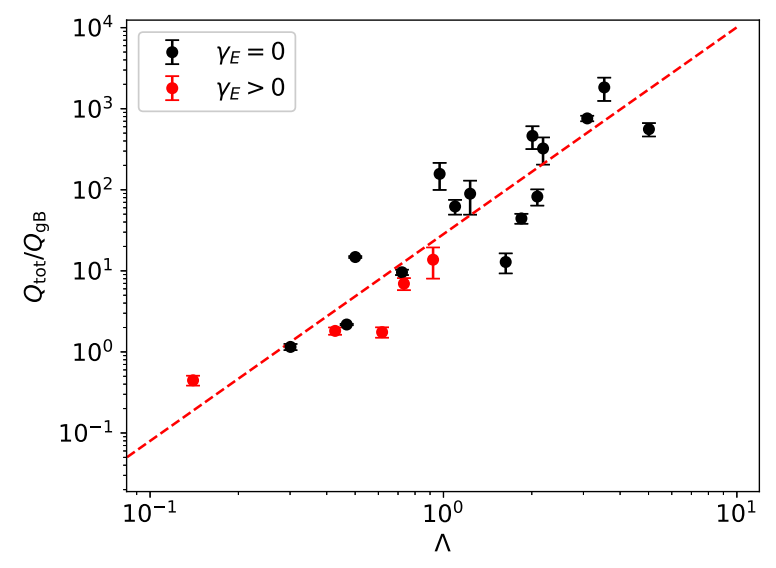


FIGURE 10. Normalised total heat flux $Q_{\rm tot}/Q_{\rm gB}$ from nonlinear gyrokinetic simulations as a function of Λ . The dashed line represents the best weighted fit, $Q_{\rm tot}=Q_0\Lambda^\alpha$, with Q_0 and α the fitting coefficients. The error bar in the heat flux is taken as the standard deviation of the heat flux time trace in the saturated phase. Black and red markers correspond to simulations without and with equilibrium flow shear, respectively.

species heat and particle fluxes with the quasi-linear predictions given by (3.7) and (3.8) is reported in the Appendix.

Turbulent transport in the nonlinear simulations of figure 10 is predominantly dominated by hybrid-KBM turbulence, but in two low β cases turbulence is from electrostatic ITG and TEM. In principle, MTMs may generate magnetic stochastic transport if the separation between the magnetic islands from the tearing perturbation is smaller than the island width (see, e.g. Doerk et al. 2011; Guttenfelder et al. 2011; Nevins, Wang & Candy 2011; Giacomin et al. 2023), but this physics is not captured here or in most other quasi-linear models since it would require predictions of the saturated magnetic island width generated by the underlying MTM instability. On the other hand, the nonlinear gyrokinetic simulations of Giacomin et al. (2024) suggest that magnetic stochastic transport should be modest on most STEP-EC-HD surfaces that have been analysed. Other simulations, however, suggest that stochastic transport may be significant in some spherical tokamak plasmas from NSTX (Guttenfelder et al. 2011) and MAST (Giacomin et al. 2023). It is entirely possible that MTM induced magnetic stochastic transport will be substantial under some plasma conditions in STEP, and investigating this is an important area for future work. It is therefore likely that the reduced turbulent transport model developed here will need to be extended to account for magnetic stochastic turbulent transport from MTMs. We note that the development of such models is an active research area (Rafiq et al. 2016; Curie et al. 2022; Hamed et al. 2023; Hornsby et al. 2024).

Figure 11(a) shows examples of the $\delta\phi$ and δA_{\parallel} contributions to the k_y spectrum of $\bar{\Lambda}(k_y)$ for the surface at $\Psi_n=0.36$ of STEP-EC-HD without and with flow shear ($\gamma_E=0$ and $\gamma_E=0.05\,c_s/a$). Both contributions to $\bar{\Lambda}(k_y)$ peak at low k_y with and without flow shear, but at $\gamma_E=0$ the peaks are significantly larger and at longer wavelength. We note that, in this local equilibrium, the δA_{\parallel} contribution to $\bar{\Lambda}(k_y)$ dominates both at $\gamma_E=0$ and $\gamma_E=0.05\,c_s/a$, highlighting the need to include δA_{\parallel} in (3.6).

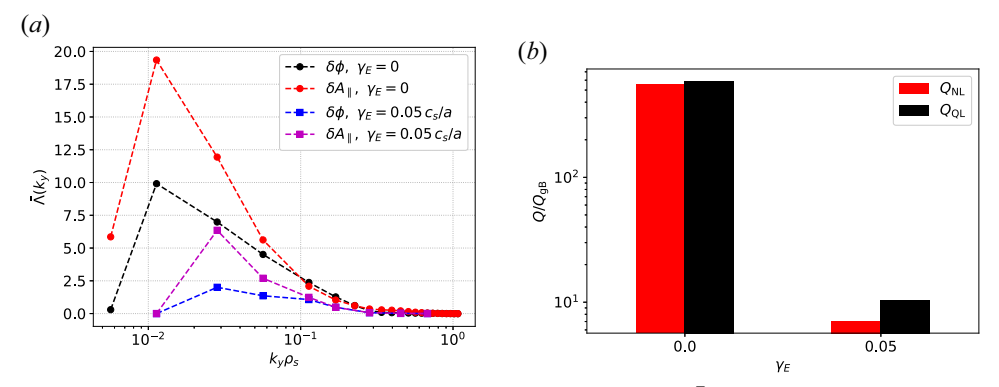


FIGURE 11. (a) Contributions of the $\delta \phi$ and δA_{\parallel} terms in (3.4) to $\bar{\Lambda}(k_y)$ without (round markers) and with (squared markers) equilibrium flow shear. The contribution from δB_{\parallel} is negligible and not shown. (b) Comparison between the nonlinear and the quasi-linear total heat flux for the two cases considered in (a). These simulations are performed at $\Psi_n = 0.36$ of STEP-EC-HD.

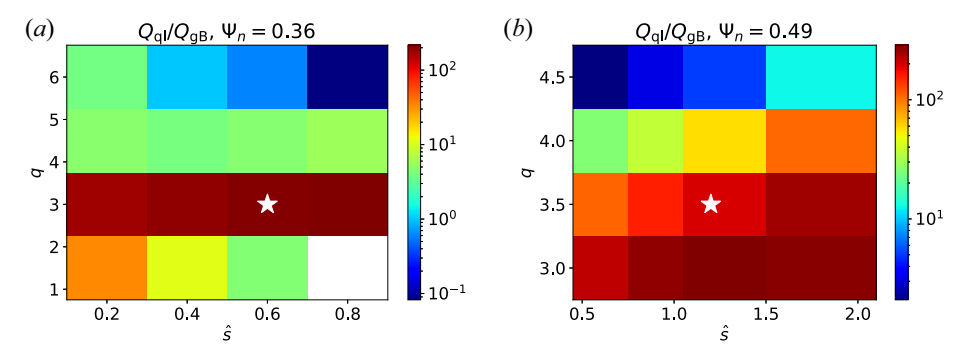


FIGURE 12. Two-dimensional (q, \hat{s}) scan of the quasi-linear heat flux (normalised to $Q_{\rm gB}$) at $\Psi_n = 0.36$ (a) and $\Psi_n = 0.49$ (b). The white stars indicate the nominal values of q and \hat{s} of the chosen STEP flat-top operating point. The simulation at $\hat{s} = 0.8$, q = 1.5 and $\Psi_n = 0.36$ is stable. In this figure, the quasi-linear heat flux is computed without equilibrium flow shear.

Figure 11(b) compares the nonlinear and quasi-linear model heat fluxes, where the reduced model used Q_0 and α in (3.1) from the fit in figure 11. The quasi-linear and nonlinear heat fluxes agree within 30%, although it is pertinent to note that both simulations were included in the database used to obtain Q_0 and α . The reduction in the heat flux attributable to flow shear approaches two orders of magnitude, and this is largely captured by the quasi-linear model. The reduction in the quasi-linear heat flux is slightly weaker than found in the nonlinear simulations, where the saturated total heat flux is 30% lower at $\gamma_E = 0.05 c_s/a$.

We underline that the nonlinear heat flux calculations in the two cases of figure 11 requires more than 5×10^5 core hours for each simulation, corresponding to a week running on 32 nodes of the ARCHER2 high performance computing facility (Edinburgh, UK); in contrast computing the quasi-linear metric takes approximately 100 core hours, corresponding to 10 minutes running on 4 nodes of ARCHER2. Computing the quasi-linear metric is at least a factor of 10^3 less expensive than computing the nonlinear heat flux.

Motivated by the analysis of Giacomin *et al.* (2024) that finds a significant influence of q on hybrid-KBM turbulence at mid-radius in STEP-EC-HD, figure 12 explores the

sensitivity of the quasi-linear heat flux to q and \hat{s} at $\Psi_n=0.36$ and $\Psi_n=0.49$. Equilibrium flow shear is not included in this two-dimensional parameter scan. At $\Psi_n=0.49$, $Q_{\rm ql}/Q_{\rm gB}$ increases monotonically as \hat{s} increases or q decreases, which is consistent with the nonlinear q scan presented in Giacomin et al. (2024). At $\Psi_n=0.36$, the dependence of $Q_{\rm ql}/Q_{\rm gB}$ on q and \hat{s} is non-monotonic, with a maximum at q=3.0; at q values higher or smaller than the nominal value, the quasi-linear heat flux decreases as \hat{s} increases. In particular, figure 12 shows the presence of a low turbulent transport regime that could be achieved by varying \hat{s} and q from their nominal values, which are denoted by the white stars in figure 12; determining whether such local equilibrium conditions can be accessed across a significant radial region, while still satisfying operational constraints, clearly requires integrated scenario modelling (Tholerus et al. 2024).

4. Flux-driven STEP simulations

Section 2.2 demonstrates that a diamagnetic level of equilibrium flow shear is insufficient to reduce the hybrid-KBM-driven heat flux below the level required to achieve a transport steady state in STEP-EC-HD with the assumed sources. The imbalance between the turbulent fluxes crossing a surface and the available sources will result in the density and temperature profiles undergoing transport evolution from this state. Other local equilibrium parameters, such as β , β' , collisionality and eventually q, \hat{s} and Δ' , are also affected by transport evolution, with the self-consistent Grad–Shafranov equilibrium and current evolving on a longer resistive time scale: local transport is affected by these local equilibrium quantities as well as the temperature and density gradients.

In this section, we report on the implementation of the quasi-linear reduced model of § 3 in the T3D code, and its exploitation to evolve the temperature and density profiles of electron and main ion plasma species in the STEP flat-top operating point introduced in § 2.

4.1. *Implementation of the reduced model in T3D*

T3D (Qian *et al.* 2022) is a transport code that has been recently developed from TRINITY (Barnes *et al.* 2010). It is a very flexible and modular tool that facilitates the implementation of new transport models. The transport equations solved by T3D are (see Barnes *et al.* 2010)

$$\frac{\partial n_s}{\partial t} + \frac{1}{V'} \frac{\partial}{\partial \Psi} (V' \overline{\Gamma_s}) = \overline{S_{n,s}}, \tag{4.1}$$

$$\frac{3}{2}\frac{\partial p_s}{\partial t} + \frac{1}{V'}\frac{\partial}{\partial \Psi}(V'\overline{Q_s}) = \frac{3}{2}n_s \sum_{u} \nu_{su}(T_u - T_s) + \overline{S_{p,s}},\tag{4.2}$$

where n_s and p_s are the density and pressure of the species s, Ψ is the flux label, V is the volume enclosed by the surface Ψ , V' is the derivative of V with respect to Ψ , Γ_s and Q_s are the total particle and heat fluxes of a given species s including the classical, neoclassical and turbulent contributions and $S_{n,s}$ and $S_{p,s}$ are the particle and the heat sources. The overline denotes a flux-surface average. The term proportional to v_{su} is the collisional energy exchange term, with v_{su} taken from Huba (1998). Density and temperature profiles are discretised on a uniformly spaced radial grid, and gradients are computed using a sixth-order finite difference scheme on interior radial grid points and a second-order finite difference scheme at the boundary. A non-zero Dirichlet boundary condition is applied at the outermost radial grid point, while the physical zero flux condition is

applied at the magnetic axis.¹⁰ Equations (4.1) and (4.2) are evolved using a semi-implicit method. Further details on the transport equations and on their numerical implementation are reported in Barnes *et al.* (2010).

Evaluating the fluxes Γ_s and Q_s in (4.1) and (4.2) requires a transport model. For instance, the coupling between T3D and GX (Mandell *et al.* 2024), a local gyrokinetic code developed to run natively on graphics processing units, allows T3D to submit nonlinear gyrokinetic simulations at each radial location to compute Γ_s and Q_s from first-principles simulations. A total number of $(N_r - 1)(N_p + 1)$ simulations per iteration is required, where N_r is the number of radial grid points and N_p is the number of evolved profiles. We note that $N_p + 1$ evaluations are required at each radial location to compute the local flux derivatives with respect to each evolved profile gradient (see Barnes *et al.* (2010) for details). The quasi-neutrality condition is applied to impose the density value of the last evolved species. Our T3D simulations for STEP use the quasi-linear reduced transport flux equations (3.7) and (3.8), which have been implemented in T3D, and exploit a coupling to GS2 for the linear calculations required to compute the quasi-linear fluxes.

The workflow of T3D-GS2 is shown in figure 13. After initialisation, where the input file (containing run configuration data, such as the radial grid resolution, the maximum number of iteration and the transport model selection), geometry, 11 initial profiles and sources are loaded, T3D-GS2 enters into the main loop, which is divided in four substeps. In the first substep, T3D writes the GS2 input files for each radial grid point and (k_y, θ_0) mode, according to the specified numerical resolutions. Several GS2 calculations are then distributed over the available MPI (Message Passing Interface) tasks. Depending on the numerical resolutions and on the number of linear gyrokinetic simulations to be performed, T3D-GS2 can efficiently scale to thousands of cores. Once all the GS2 linear simulations are completed, results are gathered and the quasi-linear fluxes are computed using (3.7) and (3.8). In the last sub-step, density and pressure profiles are evolved using (4.1) and (4.2). The transport calculation terminates when the maximum number of iterations or the maximum simulation time is reached. It is possible to restart from the final state of a previous T3D run, which is invaluable when a transport steady-state solution (characterised by power and particle losses that match sources and profiles that are constant in time) is not reached within a single run.

4.2. Evolution of density and temperature profiles in a STEP case

Here, we present results from the first flux-driven transport simulations to account for hybrid-KBM turbulence in a STEP flat-top operating point.

4.2.1. Transport simulation set-up and assumptions

In this first analysis, we have made a number of simplifying approximations that are detailed below. First, only density and temperature profiles of electrons and a single thermal ion species are evolved. The quasi-neutrality is enforced on the ion species, such that $n_i = n_D + n_T = n_e$ where $n_D = n_T = n_i/2$ with n_D and n_T being the deuterium and tritium density, respectively. The deuterium and tritium temperatures are set to be equal to each other, i.e. only one ion temperature profile is evolved, with $T_i = T_D = T_T$. We note

 $^{^{10}}$ The first radial grid point is located at $r = \Delta r/2$, where Δr is the radial grid spacing. Fluxes and gradients are evaluated on interior radial grid points (apart from the magnetic axis where fluxes vanish) up to the outermost radial grid point $r_{N_r} - \Delta r/2$. The values of density and temperature at the magnetic axis can be evaluated using the zero flux on-axis boundary condition.

¹¹Local equilibrium shaping parameters, q and \hat{s} are computed from the initial state and kept constant during the T3D simulation, while local β' is updated every time step consistently with the pressure profile. There is a plan in the future to allow the magnetic equilibrium in T3D to be recomputed self-consistently from the pressure profile every N time steps.

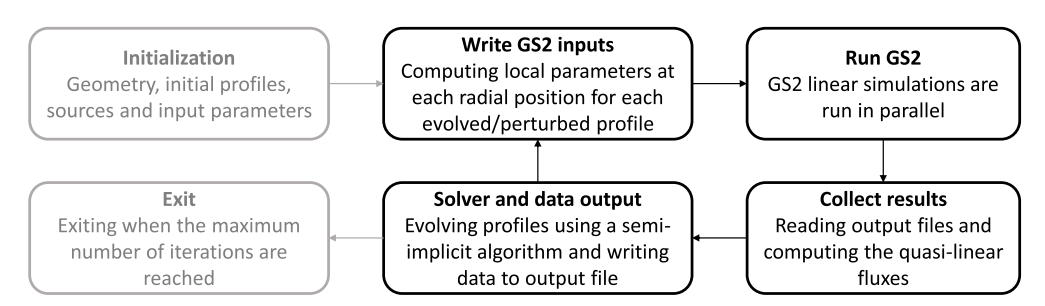


FIGURE 13. Workflow of T3D-GS2. The main cycle is decomposed in four main blocks (in black): writing GS2 input files, running GS2, computing the quasi-linear heat flux and evolving the density and temperature profiles. The blocks in grey are executed only once per simulation.

that the nonlinear gyrokinetic simulations used to develop the reduced model parameters, Q_0 and α in (3.1), excluded impurities, helium ash and fast α particles. It will be an important future research direction to include these additional ion species in nonlinear gyrokinetic simulations, and to extend the reduced model to accommodate their impacts on the turbulent fluxes. Second, the geometrical shaping parameters, q and \hat{s} are held constant while evolving the pressure profile. If the initial and final pressure profiles are similar, the magnetic equilibrium should change only slightly, although even small variation of safety factor or magnetic shear may impact turbulence (see, e.g. the dependence on the safety factor in figure 12). On the other hand, the value of β' is evolved self-consistently with the pressure profile in our T3D simulations, and this is known to have a strong impact on turbulence in STEP-EC-HD (see Giacomin et al. 2024). Finally, the equilibrium flow shear has been computed from (2.1), where E_r is taken from the JINTRAC STEP flat-top operating point, and has been kept constant as the kinetic profiles evolve. There is no external torque in STEP, so equilibrium flow shear is relatively small ($\gamma_E \lesssim 0.05 \, c_s/a$). Sensitivity to γ_E is addressed specifically through T3D simulations with $\gamma_E(r)$ varied by 40% around $\gamma_E^{\rm dia}$. In addition, the model parameters α and Q_0 are varied within 20%(which is the uncertainty given by the weighted/unweighted fit in figure 10) to investigate the impacts of uncertainties on these parameters. The reference case is performed using the values of Q_0 and α from the fit in § 3, and setting $\gamma_E = [0.01, 0.01, 0.02, 0.03, 0.05] c_s/a$ at r/a = [0.16, 0.33, 0.49, 0.65, 0.82], respectively.

Our T3D simulations use six radial grid points uniformly distributed over the radial domain, extending from the magnetic axis to r/a = 0.9 close to the pedestal top. At each radial position and for each profile, a total of $n_{k_y} \times n_{\theta_0} = 12 \times 6 = 72$ linear modes are evolved, using a non-uniform grid spacing in k_v and θ_0 to improve resolution at low k_v and low θ_0 , which is the region contributing most strongly to the quasi-linear metric. A minimum $k_y \rho_s$ is imposed to resolve only toroidal mode numbers n > 1, and its value depends on radial location and plasma profiles. Each mode is evolved by an independent GS2 simulation in ballooning space. The GS2 simulations are performed using 33 grid points along θ , 24 pitch angles and 10 energy grid points. The total number of GS2 simulations in ballooning space carried out at each step is $N = (N_r - 1)(N_p + 1)n_{k_r}n_{\theta_0} =$ 1440, where $N_p = 3$ as n, T_e and T_i are evolved here. The GS2 simulations are performed in parallel depending on the number of available MPI tasks. The auxiliary heating power density profile from electron cyclotron resonant heating ($P_{EC} = 150 \text{ MW}$ in total), radiated power density profile ($P_{\text{rad}} = 340 \text{ MW}$ in total) and particle source from pellet injection (corresponding to a fuelling rate $\sim 10^{22}$ particles s⁻¹) are taken from the JINTRAC simulation of STEP-EC-HD (see Tholerus et al. (2024) for details), and kept constant

throughout the T3D transport calculation. Fusion α -particle heating and collisional energy exchange contributions to (4.2) evolve with the density and temperature profiles and are calculated self-consistently. The ion density is multiplied by a dilution factor, $f_{\text{He}} = 0.9$, when computing the fusion power in order to account for the dilution effect from helium ash. Motivated by the presence of subdominant MTM turbulence in the STEP initial condition (Giacomin *et al.* 2024), a small additional Rechester-Rosenbluth-like contribution is included in the electron heat flux proportional to $(a/L_{Te})^3$ (see Doerk *et al.* 2011). This helps convergence, while it has a negligible impact in the final T3D steady state. Neoclassical transport is included in the following T3D simulations and is computed using the neoclassical code NEO (Belli & Candy 2008).

4.2.2. Transport simulation results

Figure 14 compares the initial temperature, density and pressure profiles and their gradients taken from the JINTRAC STEP flat-top operating point with the corresponding profiles from the final state of the reference T3D simulation. Fluxes and gradients in T3D are computed at the mid-point between each radial grid point. The final electron temperature profile values are lower than in the initial condition, with the largest reduction occurring near the magnetic axis where T_e decreases by approximately 10%. The final normalised logarithmic electron temperature gradient, a/L_{T_e} , oscillates radially around its initial profile, and the largest difference is in the inner core, where the final electron temperature profile is flatter than the initial one.

A significant reduction is observed in the ion temperature profile for r/a < 0.4, where there is a 20% reduction in T_i near the magnetic axis. On the other hand, the initial and final ion temperature profiles are very similar in the outer core at r/a > 0.5. The ITG is smaller than the initial temperature gradient over the entire radial domain, except near $r/a \simeq 0.8$, where it is slightly larger. We note that the initial ion temperature profile is significantly higher than the electron temperature despite this flat-top operating point being dominated by electron heating: this arises because the transport model used to design STEP-EC-HD assumed negligible turbulent ion heat transport. This feature is not recovered in the T3D calculation using our reduced model for hybrid-KBM turbulence, where the ion turbulent transport is non-negligible and the final T_i and T_e profiles are very similar, with a/L_{T_i} reducing significantly compared with its initial value between $r/a \simeq 0.4$ and $r/a \simeq 0.65$.

The final T3D electron density is close to the initial profile for r/a < 0.6, but higher for r/a > 0.6: i.e. there is a small increase in the edge density gradient for $r/a \simeq 0.8$ and a relaxation of the gradient around $r/a \simeq 0.65$. We note that the density increase occurs in proximity of the maximum density source due to pellet injection, shown in figure 14(c). The particle confinement time evaluated from the T3D steady-state solution is $\tau_p = \int n_e \, dV / \int S_n \, dn = 12.5 \, \text{s}$, which is close to that assumed in STEP-EC-HD (Tholerus et al. 2024). We highlight that the T3D steady-state ion temperature and density gradients at $r/a \simeq 0.8$ are larger than in the initial condition from STEP-EC-HD. This may appear counter-intuitive, especially given that the reduced model heat and particle fluxes are much larger than the available sources at the STEP-EC-HD initial condition, as illustrated in figure 16. On the other hand, the dependence of the turbulent fluxes on the temperature and density gradients is non-monotonic in STEP-EC-HD because of the stabilising β' effect, as pointed out in Giacomin et al. (2024). The profile evolution in the initial phase leads to a steepening of temperature and density profile in the outer core region, which causes a local increase of the β' value and a subsequent reduction of turbulent fluxes, thus sustaining larger density and temperature gradients in the outer core region. We note, however, that the variation of other parameters, such as β and collisionality, the evolution

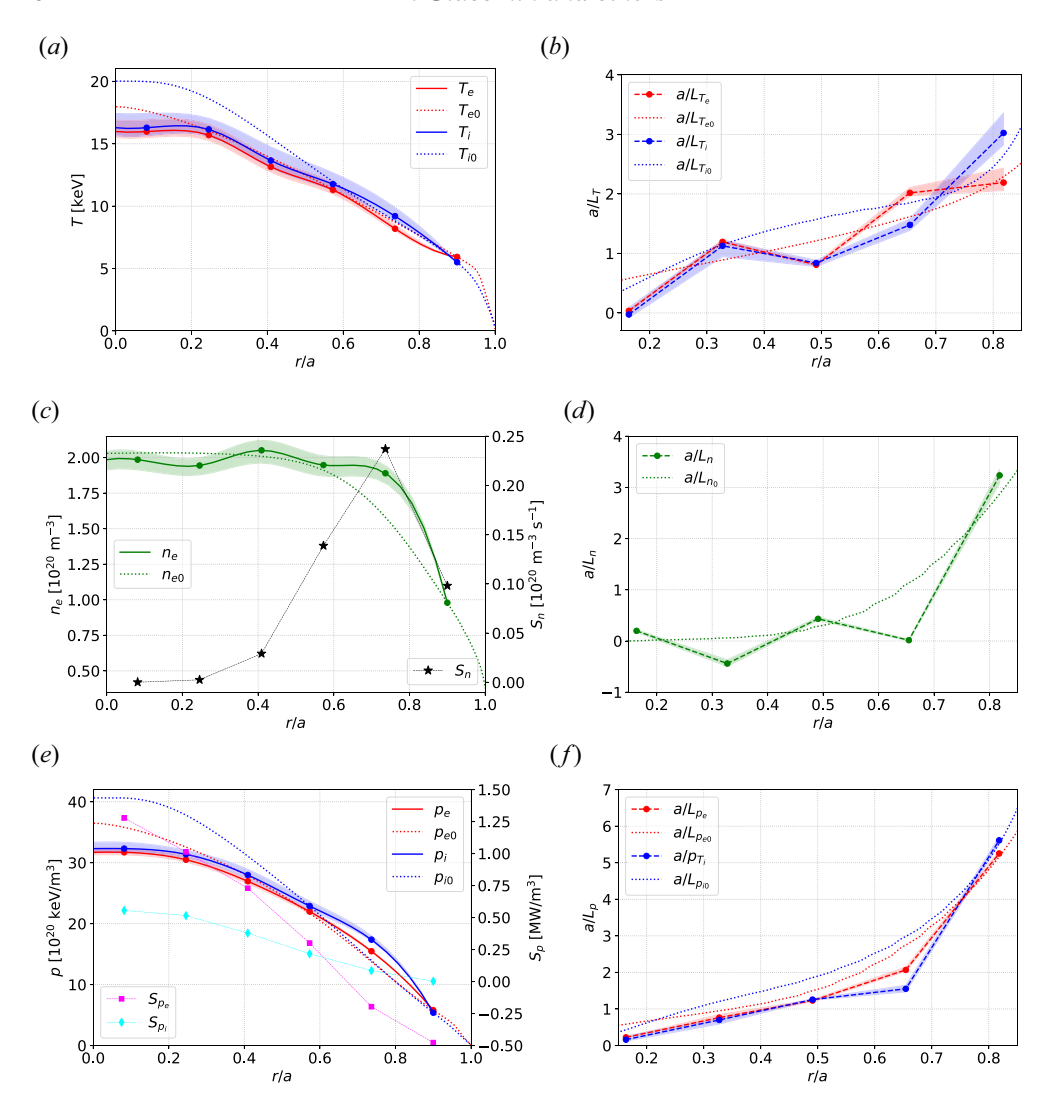


FIGURE 14. Comparison of initial (dotted lines) and final (solid lines) temperature (a), density (c) and pressure (e) profiles as well as their inverse gradient scale lengths (b,d,f). The initial profiles are taken from the JINTRAC analysis (Tholerus $et\ al.\ 2024$). The round markers denote the position of the radial grid points in the T3D grid. The value of the density and pressure at the outermost radial grid point is imposed by the finite Dirichlet boundary condition. The shaded area represents the profile variation corresponding to a $\pm 40\%$ variation in γ_E and a $\pm 20\%$ variation in Q_0 and α . The solid line represents an interpolation through the T3D radial grid points. The particle source (star markers) as well as the electron (square markers) and ion (diamond markers) total power sources are shown in (c,e).

of the fusion power and the contribution from the neoclassical fluxes make the dynamics regulating the profile evolution strongly nonlinear: this effect cannot be solely explained by the dependence of turbulent fluxes on gradients.

Figure 14 shows also a comparison between the initial and final pressure profile: the reduced final pressure for r/a < 0.6 is consistent with lower T_e and T_i in this region of the plasma; for r/a > 0.6 both the electron and ion final pressure profiles are larger

than the initial profiles, mostly because of the increased density. If we do not separate transport and radiation losses, the energy confinement time using the final steady-state pressure profile gives $\tau_E = \frac{3}{2} \int p \, dV/P_{\rm net} = 1.5 \, \text{s}$, with $P_{\rm net} = P_\alpha + P_{\rm EC}$. If we exclude radiation losses from the net loss power using $P_{\rm net}^* = P_\alpha + P_{\rm EC} - P_{\rm rad}$, this gives $\tau_E^* = \frac{3}{2} \int p \, dV/P_{\rm net}^* = 4.6 \, \text{s}$. These energy confinement times are similar to those assumed in the original STEP flat-top operating point 12 (Tholerus *et al.* 2024). We highlight, however, that the radial domain evolved by these T3D simulations does not include the pedestal region. The outermost radial grid point boundary condition of the density and temperature is taken from near the pedestal top of the JINTRAC initial profiles (see figure 14); the pedestal model used in the JINTRAC modelling of this STEP flat-top operating point is described in Tholerus *et al.* (2024). Any variation of the pedestal top, and therefore of the outer boundary condition, is likely to impact core transport and the energy confinement time. Assessing the sensitivity on the outer boundary condition, i.e. on the density and temperature values at the pedestal top, is clearly a very important topic for future investigation.

The shaded area in figure 14 indicates the range of profiles variation obtained from T3D simulations with local values of γ_E varied by $\pm 40\,\%$ from the nominal value, and also includes additional T3D simulations where Q_0 and α are varied by $\pm 20\,\%$ to assess the impacts of uncertainties in the reduced model parameters. The variation in the density and temperature profiles is comparatively small, which may seem surprising given the large sensitivity of fluxes to γ_E in STEP-EC-HD. This relatively weak sensitivity of the kinetic profiles on the shearing rate can be explained (i) by T3D converging to a regime where the hybrid-KBM turbulence is closer to marginal, especially at low k_y , in the transport steady state, owing reductions of the density gradient in the core and increases in β' at the edge; and (ii) by large transport stiffness, where small variations in the temperature and density gradients lead to large changes in the turbulent flux. High transport stiffness improves the robustness of the T3D steady state.

Figure 15 shows the time evolution of the density and temperature gradients as well as of the power and particle losses over the duration of the T3D reference simulation. The time traces can be divided in three main phases. The first phase is very short (0 < $t \lesssim 0.1$ s, 50 solver iterations) and is characterised by a fast evolution of the profiles that leads to a substantial reduction of power and particle losses. This fast initial phase is caused by the strong initial particle and power imbalance, as shown in figures 16(a) and 16(c). The second phase $(0.1 \lesssim t \lesssim 9 \text{ s}, 100 \text{ solver iterations})$ is characterised by a slow evolution of gradients and fluxes towards a steady-state solution. In this phase, the particle fluxes at $r/a \simeq 0.16$ and $r/a \simeq 0.33$ drop to negligible values, which is consistent with an approach to steady state with no particle source in the core. There is a transitory ripple in the time evolution of the power and particle losses at $r/a \simeq 0.33$ and $r/a \simeq 0.49$, while the density and temperature gradients vary smoothly; this is caused by low k_v hybrid-KBMs being stabilised or destabilised while T3D profiles are slowly converging to a steady-state solution, and it is amplified by stiff transport. Apart from the ripple and slow increase of particle flux at $r/a \simeq 0.5$, power and particle losses do not vary significantly in the second phase. The final phase (40 solver iterations) reaches the transport steady state, where the kinetic gradients, power and particle losses are constant in time. Figure 16 shows excellent agreement between transport losses and sources in the T3D transport steady state.

¹²The T3D steady-state energy confinement time is slightly higher than in the original STEP-EC-HD ($\tau_E = 1.24 \text{ s}$ and $\tau_E^* = 4.20 \text{ s}$) because of the larger density in the outer core, which leads to a slightly larger $\int p \, dV$.

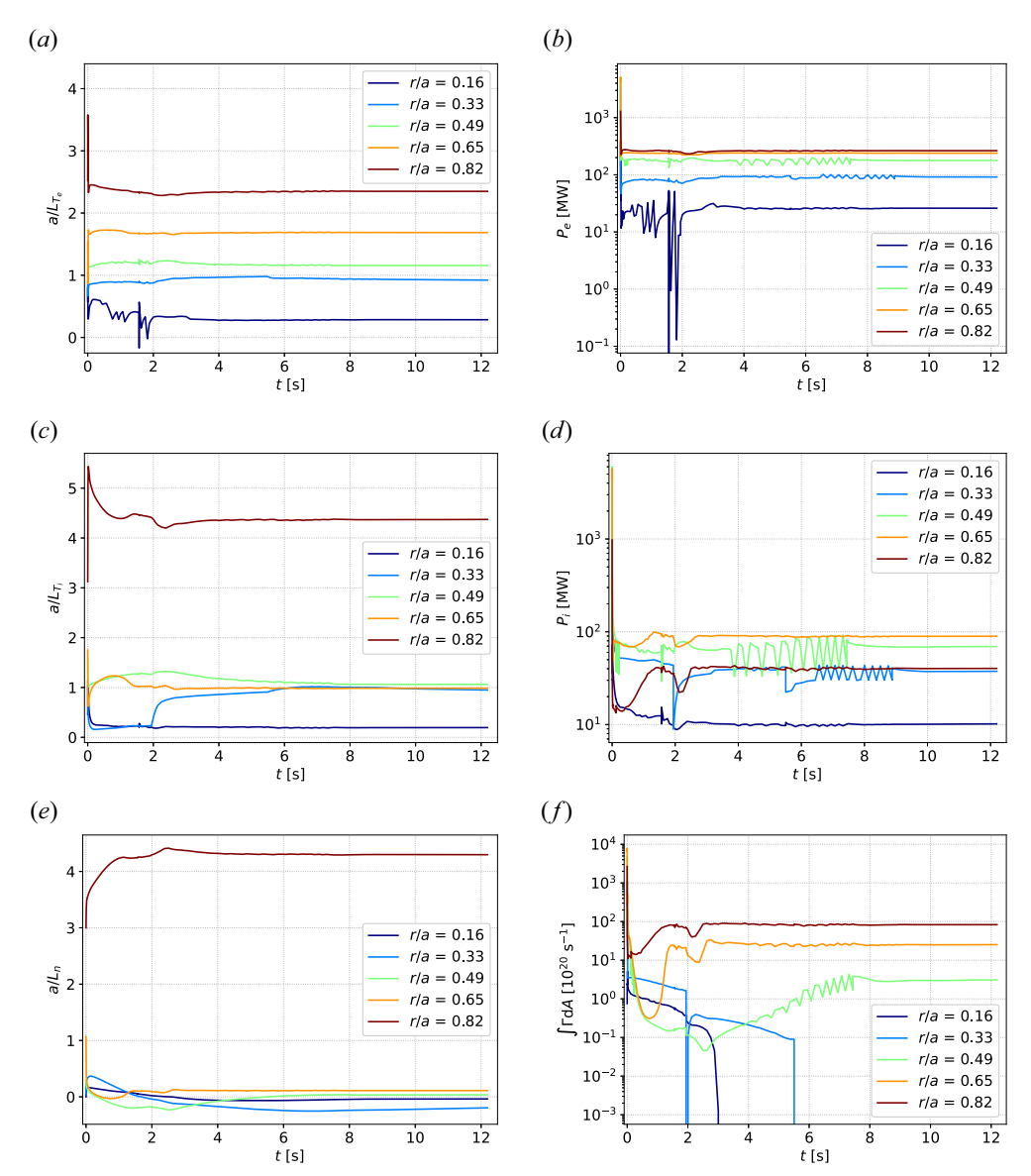


FIGURE 15. Time evolution of the density and temperature gradients as well as of the power and particle losses in the reference T3D simulation. The initial profiles are taken from the JETTO STEP-EC-HD flat-top operating point. Different colours represent different radial surfaces (fluxes and gradients in T3D are computed at the mid-point between each radial grid point).

The heating power density radial profiles from auxiliary and α -particle heating, collisional exchange and radiation are shown in figure 17(a) for the final T3D steady state, while the evolution of the fusion power is shown in figure 17(b). Consistently with the pressure profile evolution, the fusion power rapidly decreases in the initial phase, which is followed by a slower evolution. The final fusion power is approximately 10% smaller than its initial value.

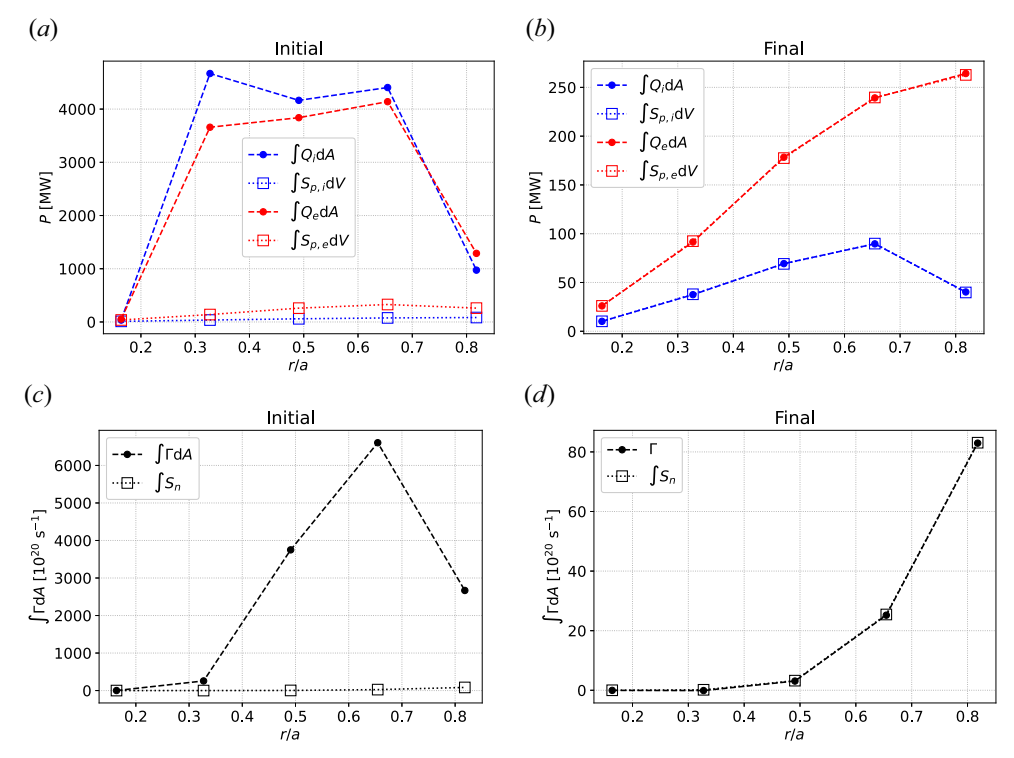


FIGURE 16. Power (a,b) and particle (c,d) balance in the initial and final states of the reference T3D simulation. Heat and particle sources are denoted with open markers, and heat and particle losses with solid markers. The initial state is taken from JINTRAC-JETTO STEP flat top.

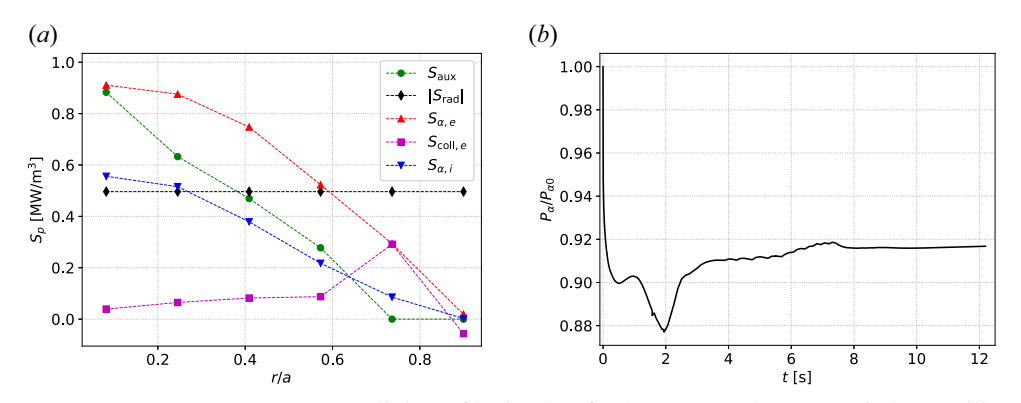


FIGURE 17. (a) Power source radial profile in the final T3D steady state of the auxiliary heating (S_{aux}) , α -particle heating $(S_{\alpha,e})$ and $S_{\alpha,i}$, collisional exchange $(S_{\text{coll},e}) = -S_{\text{coll},i}$ and radiation (S_{rad}) . (b) Fusion power evolution in the reference T3D simulation. The fusion power is normalised to its initial value of 1.7 GW.

5. Gyrokinetic analysis of the T3D transport steady state

The aim of this section is to verify whether fluxes from nonlinear gyrokinetic simulations remain consistent with our reduced model in the transport steady state from T3D. This verifies whether the quasi-linear reduced transport model of (3.7) and (3.8)

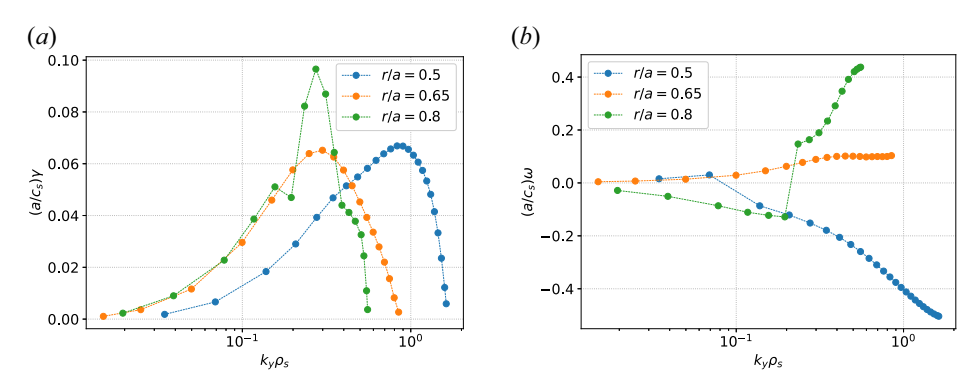


FIGURE 18. Growth rate (a) and mode frequency (b) as functions of k_y at r/a = 0.5 (blue dots), r/a = 0.65 (orange dots) and r/a = 0.8 (green dots) from linear simulations of the new STEP density and temperature profiles.

faithfully describes turbulent transport in an equilibrium that was not in the database used to tune the model parameters in § 3. This test is performed at the three outermost T3D radial grid points, i.e. $r/a \in \{0.5, 0.65, 0.8\}$, which are the most critical surfaces for fusion performance.¹³

5.1. Linear analysis

Linear simulations are performed on these three surfaces with GS2, using numerical resolutions similar to those used in § 2.1, except setting $n_{\text{period}} = 32$ at r/a = 0.5. The dominant mode growth rates and mode frequencies are shown as functions of k_y in figure 18. The mode frequency at r/a = 0.5 shows a discontinuity between $k_y \rho_s = 0.15$ and $k_y \rho_s = 0.2$, which corresponds to a transition of the dominant mode from hybrid-KBMs to MTMs. The $\delta \phi$ parallel mode structures at $k_y \rho_s \simeq 0.07$ and $k_y \rho_s \simeq 0.83$, corresponding to the fastest growing hybrid-KBM and MTM respectively, are shown in figure 19. The hybrid-KBM eigenfunction is narrow in θ and has even parity, while the MTM eigenfunction has odd parity and is much more extended in θ . A sign change on the mode frequency is also observed in figure 18 at r/a = 0.8 around $k_y \rho_s \simeq 0.2$. In this case, however, the parallel structures of modes with positive and negative frequencies are similar. This is consistent with the complex nature of the hybrid-KBM, involving both trapped electron and ion dynamics, discussed in Kennedy *et al.* (2023).

Figure 20 shows a comparison of the growth rate values between the initial and final STEP plasma profiles at r/a = 0.5, r/a = 0.65 and r/a = 0.8. Beyond the difference on the dominant instability at r/a = 0.5 (the hybrid-KBM and MTM instabilities dominate in the original STEP case and in the new T3D steady state, respectively), a strong stabilisation at low k_y and a substantial growth rate maximum shift at higher k_y are observed in the new T3D steady state. At both r/a = 0.65 and r/a = 0.8 cases, where the dominant instability remains the hybrid-KBM, there is a clear reduction of the growth rates across most of the spectrum, including at low k_y which typically dominates the turbulent fluxes. This linear comparison underlies the substantial reduction of turbulent flux predictions by the reduced transport model between the initial condition and the transport steady state. This will now be compared with nonlinear gyrokinetic simulations.

¹³The pressure profile in the core for r/a < 0.4 is rather flat and any failure of the reduced transport model in this region should only weakly influence fusion performance.

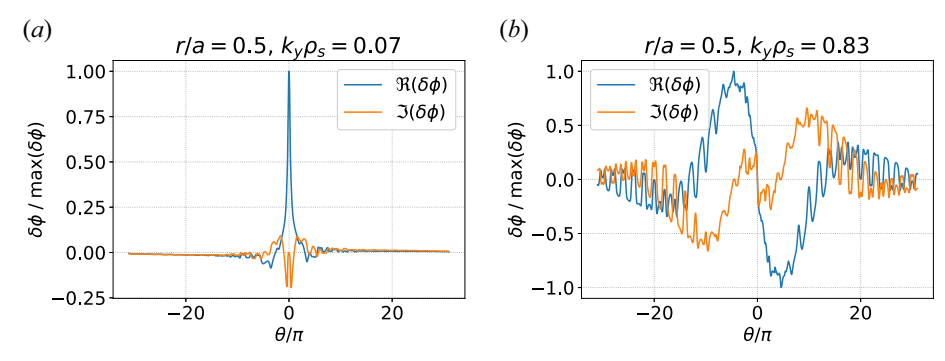


FIGURE 19. Parallel mode structure of $\delta \phi$ at $k_y \rho_s \simeq 0.07$ (a) and $k_y \rho_s \simeq 0.83$ (b) corresponding to the maximum growth rate of the hybrid-KBM and MTM instability, respectively, at r/a=0.5 of the new STEP profiles obtained from the T3D reference simulation.

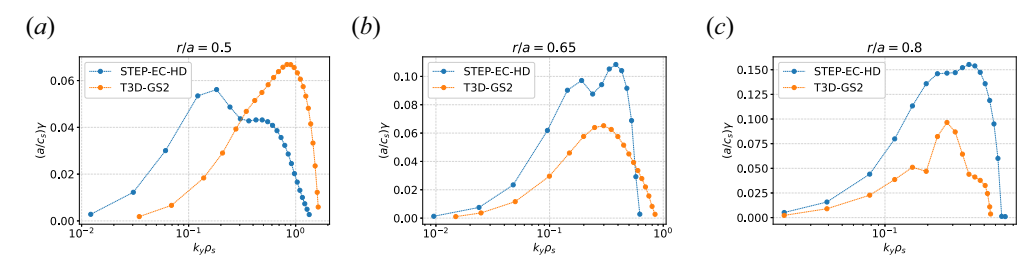


FIGURE 20. Growth rate comparison between the initial (STEP-EC-HD) and final (T3D-GS2) profiles at r/a = 0.5 (a), r/a = 0.65 (b) and r/a = 0.8 (c).

r/a	$\Delta k_y \rho_s$	$k_{y,\max}\rho_s$	$\Delta k_x \rho_s$	$k_{x,\max}\rho_s$	n_{θ}	n_{μ}	n_v
0.50	0.035	1.65	0.030	2.0	32	16	28
0.65	0.030	1.10	0.026	1.70	32	16	28
0.80	0.019	0.90	0.034	2.21	64	16	28

TABLE 3. Numerical resolutions used in nonlinear GENE simulations on three surfaces from the T3D transport steady state, r/a = [0.5, 0.65, 0.8].

5.2. Nonlinear analysis

Here, we briefly show results from nonlinear gyrokinetic simulations performed using GENE at r/a = [0.5, 0.65, 0.8] in the T3D steady-state solution: these simulations used the numerical resolutions listed in table 3. These simulations include equilibrium flow shear with $\gamma_E = [0.02, 0.03, 0.05] c_s/a$ at r/a = [0.5, 0.65, 0.8], respectively. Figure 21 plots the total heat and particle transport losses across these three surfaces in the transport steady state, comparing values from the quasi-linear model in T3D with neoclassical and turbulent fluxes computed using NEO and GENE.

At r/a = 0.5 and r/a = 0.65, figure 21 shows relatively good agreement between the nonlinear gyrokinetic heat flux and the reduced transport model in T3D. The neoclassical heat flux is negligible at these radial locations. There is also good agreement between the gyrokinetic and reduced model particle losses here, and we note that both neoclassical and turbulent particle fluxes are negligible at r/a = 0.5.

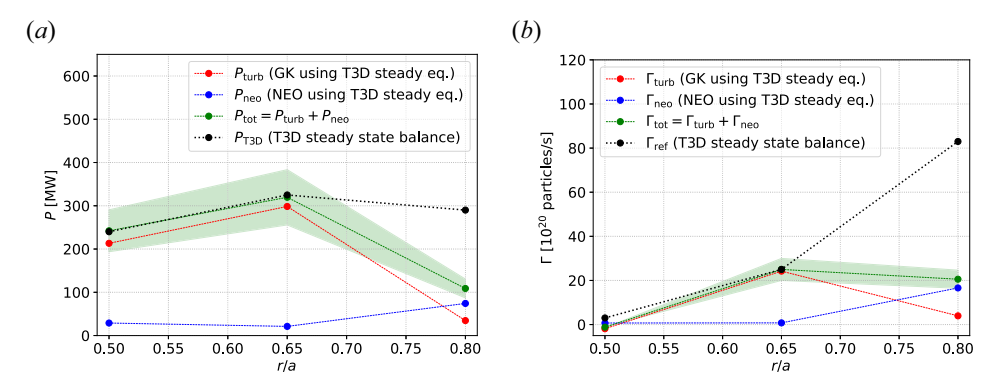


FIGURE 21. Turbulent (red dots), neoclassical (blue dots) and total (green dots) power (a) and particle (b) losses at r/a = 0.5, r/a = 0.65 and r/a = 0.8 of the new STEP profiles, compared with the expected heating power and particle fuelling from the original STEP case (black dots). The green shaded area corresponds to a $\pm 20\%$ of the total heat (a) and particle (b) transport. The turbulent fluxes are evaluated from GENE nonlinear gyrokinetic simulations and the neoclassical fluxes are evaluated from NEO simulations, both considering the T3D steady-state profiles.

Turbulent transport in the GENE nonlinear simulation at r/a=0.5 is mainly driven by hybrid-KBMs, in spite of linearly dominant MTMs (see figure 18): the nonlinearly dominant mode fields $\delta\phi(\theta)$ and $\delta A_{\parallel}(\theta)$ have even and odd parity, respectively. Good agreement in figure 21 at r/a=0.5 suggests that transport from these hybrid-KBMs is captured faithfully by the quasi-linear reduced transport model.

At r/a = 0.8, the quasi-linear model overestimates the heat and particle fluxes from the nonlinear simulation, despite turbulent transport being solely driven by hybrid-KBMs. Turbulent fluxes should therefore be described well by the quasi-linear model. The disagreement might be due to some inaccuracy affecting the quasi-linear model, as visible in figure 10 where a few points exhibit order of magnitude differences between the quasi-linear and the nonlinear heat flux predictions. In addition, the local equilibrium at r/a = 0.8 might be near a marginal state where a small increase in drive can boost the turbulent fluxes significantly: this marginal condition, where simulations are more difficult and nonlinear effects intrinsically important, might not be described well by the quasi-linear model, although further investigations, which are outside the aim of this work, would be required before drawing firm conclusions. We note that transport stiffness should allow particle and power balance to be restored with a modest increase in the drive and minimal impact on the overall density and temperature profiles. In fact, transport stiffness makes flux-driven simulations less sensitive to input parameters and improves the robustness of the steady-state profile predictions.

In summary, figure 21 shows that gyrokinetic transport fluxes for the T3D transport steady state in STEP are broadly consistent with the quasi-linear reduced transport model of (3.7) and (3.8). This gives confidence in the validity of the reduced model within the parameter space explored in this T3D transport simulation. It is important to stress, however, that this is a first iteration to develop a suitable reduced model for STEP: further guidance from higher-fidelity nonlinear gyrokinetic simulations will be required to overcome important limitations of the reduced transport model presented here, including the absence of fast α effects. Nevertheless the reduced model and T3D-GS2 are powerful tools that could be further developed and used more extensively, together with existing

integrated modelling codes, to assist in the design of new STEP plasmas and flat-top operating points.

6. Conclusions

Nonlinear gyrokinetic calculations have demonstrated the need to account for transport from hybrid-KBM turbulence in the design of STEP plasma scenarios (Giacomin et al. 2024). Scenario design therefore needs to model the transport from such turbulence at modest computational cost, which motivates the development of a new reduced transport model to describe hybrid-KBM turbulence in STEP-like regimes. The reduced transport model developed here is inspired by quasi-linear theory, and gives the transport fluxes of (3.7) and (3.8). The quasi-linear model is applied to the total heat flux through a quasi-linear metric, Λ , that lies at the heart of the model. The quantity Λ is computed directly from linear gyrokinetic calculations: it is fully electromagnetic with contributions from all three fields and it exploits the dependence of linear modes on the ballooning parameter, θ_0 , to include the impact of flow shear on turbulent saturation. To this point the model is rather general, but it contains two free parameters, Q_0 and α , that link Λ to the total heat flux. Here, the reduced model total heat flux is optimised for hybrid-KBM turbulence by tuning these parameters to best match results from a set of nonlinear gyrokinetic simulations for STEP-relevant parameters, as shown in figure 10. The saturation rule in (3.1) is in itself rather general, and with suitable different choices of coefficients Q_0 and α it may also be applicable to other turbulence regimes.

The new quasi-linear model is first applied to explore the dependence of STEP transport fluxes on safety factor and magnetic shear. This recovers the strong non-monotonic dependence of transport fluxes on q that was previously revealed on a mid-radius surface using nonlinear gyrokinetic simulations Giacomin $et\ al.\ (2024)$. Evaluating the quasi-linear fluxes requires only linear gyrokinetic calculations, which are considerably cheaper computationally than nonlinear gyrokinetics. A new reduced model with sufficient fidelity to replace nonlinear gyrokinetics offers enormous potential benefits, including making the exploration of larger regions of STEP parameter space more tractable.

This reduced transport model is implemented in T3D (Qian et al. 2022), which includes a flexible transport solver based on the algorithm developed for the TRINITY code (Barnes et al. 2010). Implementation of the model is achieved by coupling T3D to the local gyrokinetic code GS2, which is run linearly to determine the quasi-linear fluxes (see figure 13 for a summary of the code workflow). The T3D-GS2 calculations are performed from an initial condition set to the STEP-EC-HD flat-top operating point Tholerus et al. (2024). To test the sensitivity of the resulting transport steady state to uncertainties, calculations are performed with reasonable variations in the reduced model parameters Q_0 and α , and in flow shear. These initial T3D-GS2 simulations converge to a transport steady state, with density and temperature profiles that are only weakly affected by the aforementioned variations (see shaded area in figure 14). The robustness of the solution is likely due to profile relaxation in the presence of highly stiff transport, which is not captured in gradient-driven simulations (Giacomin et al. 2024). The transport steady-state pressure profile from T3D is 20 % lower on-axis but broader than the initial STEP-EC-HD pressure profile, and the energy confinement times are similar ($\tau_E^* = 4.6 \text{ s}$ in the T3D steady state, while $\tau_E^* = 4.2 \text{ s}$ in the STEP-EC-HD). The total fusion power in the T3D steady state is lower than in STEP-EC-HD by 10 %, although we note that fusion power is a highly sensitive parameter that may change significantly when assumptions from this first physics-based transport calculation are relaxed.

In order to verify whether turbulent transport remains consistent with the reduced model fluxes in the T3D solution and with the modelled sources and sinks, nonlinear gyrokinetic

calculations were performed at the three outermost radial grid points of the T3D transport steady state, at r/a = [0.5, 0.65, 0.8]. These surfaces are the most critical for fusion performance. The dominant microinstabilities are similar to those in STEP-EC-HD, with hybrid-KBMs dominant at r/a > 0.6 and MTMs dominant at r/a = 0.5. Hybrid-KBM linear growth rates, including at low k_y , are lower in the transport steady state than in the STEP-EC-HD initial condition, which is consistent with the substantial reduction in turbulent transport found nonlinearly. It is important to point out that local gyrokinetics appears to describe turbulence well in the new T3D steady-state solution, where radial turbulent structures are much smaller and transport is much closer to threshold than found in STEP-EC-HD. This nonlinear gyrokinetic analysis supports that (i) the reduced model is a reasonable description of nonlinear fluxes found on these surfaces and (ii) the T3D steady state is compatible with the modelled sources. The reduced transport model developed here could be used more routinely to account for hybrid-KBM turbulent transport in STEP scenario development, which is one of STEP most pressing needs.

First flux-driven calculations using this physics-based reduced model suggest that a transport steady state exists for STEP, which is broadly compatible with assumed sources in STEP-EC-HD and delivers close to the target fusion power. The β' stabilisation at the edge appears to play a key role in sustaining the stored energy. We highlight, however, that these initial calculations have made some simplifying assumptions that could impact on the transport steady state: (i) most magnetic equilibrium parameters are held constant: shaping, safety factor (and \hat{s}), but not β' which evolves with the pressure profile, (ii) impurities (e.g. from thermalised helium) and fast- α particles are neglected, (iii) the radial electric field is held constant and (iv) external heat and particle sources and radiation are constant while fusion α -heating and electron—ion exchange evolve with the kinetic profiles. We also highlight that a route to access this transport steady state has not been demonstrated.

In the reference T3D simulation, quasi-linear heat fluxes are computed approximately 300 times at each radial location before the transport steady state is reached, at a total computational cost of approximately 10⁵ core hours. If fluxes were computed using nonlinear local gyrokinetics, this computational cost would have exceeded 10⁸ core hours as a single calculation requires more than 10⁵ cores hours in STEP-like regimes. Starting from the reduced model transport steady state from T3D as an initial condition, however, should significantly reduce the computational cost of the nonlinear gyrokinetic approach to such a flux-driven calculation. It can be envisaged that scenario design for future machines, including STEP, will benefit from exploiting a hierarchy of tools similar to that outlined in figure 22: integrated modelling codes like JETTO, with lower computational cost and fidelity transport models, providing initial profiles; refinement of transport predictions with intermediate-fidelity physics-based models like the quasi-linear reduced model in T3D-GS2: and further honing with higher-fidelity flux-driven codes like TANGO-GENE. T3D-GX or PORTALS-CGYRO, based on nonlinear gyrokinetic fluxes. This approach may also be used to improve the fidelity of models used in integrated modelling, e.g. by implementing the reduced transport model of the intermediate approach directly into JETTO (which would require either using a fast linear eigensolver or building a surrogate model).

This work motivates many exciting future research directions. The reduced model can be exploited to seek improved STEP operating points, e.g. through optimising the q profile or other equilibrium properties. More sophisticated and demanding higher-fidelity flux-driven calculations are needed where auxiliary heating, current drive, magnetic equilibrium and flow shear are recomputed self-consistently with the kinetic profiles. The reduced model should be extended to include impurities and fast α -particles, and

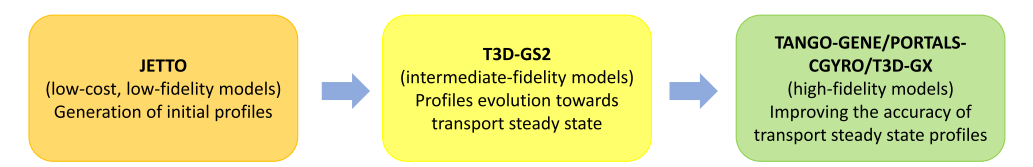


FIGURE 22. Hierarchy of tools that can be used in tandem to design plasma scenarios, involving lower cost and fidelity (left) and higher cost and fidelity (right) transport simulations. T3D-GS2 with the quasi-linear model provides an intermediate step between computationally cheap low-fidelity and more demanding high-fidelity transport simulations using nonlinear gyrokinetics.

it may also be necessary to include magnetic stochastic turbulent transport from MTMs if these become dominant when hybrid-KBMs are suppressed. A further key application for T3D-GS2 and the new model will be to explore the STEP I_p ramp-up phase, and to help find a route to access the high performance flat-top steady state. Last, but certainly not least, it will be important to seek suitable experimental regimes where this new quasi-linear model can be validated.

Acknowledgements

We would like to thank T. Adkins, E. Belli, J. Candy, B. Chapman-Oplopoiou, A. Di Siena, T. Görler, P. Ivanov, H. Meyer and F. Sheffield for useful discussions.

Editor Paolo Ricci thanks the referees for their advice in evaluating this article.

Funding

This work has been funded by the Engineering and Physical Sciences Research Council (grant numbers EP/R034737/1 and EP/W006839/1) and by STEP, a UKAEA programme to design and build a prototype fusion energy plant and a path to commercial fusion. Simulations have been performed on the ARCHER2 UK National Supercomputing Service under the project e607, on the Cambridge Service for Data Driven Discovery (CSD3) facility operated by the University of Cambridge Research Computing Service that is partially funded by the Engineering and Physical Sciences Research Council (grant EP/T022159/1) and on the Viking cluster that is a high performance compute facility provided by the University of York.

Declaration of interests

The authors report no conflict of interest.

Data availability

To obtain further information on the data and models underlying this paper please contact PublicationsManager@ukaea.uk.

Appendix. Quasi-linear species flux contributions

The quasi-linear reduced transport model is developed starting from the total heat flux, as detailed in § 3 (see (3.1)). Each species particle and heat flux contribution is then determined from the quasi-linear weights $Q_{l,s}(k_y, \theta_0)/Q_l(k_y, \theta_0)$ and $\Gamma_{l,s}(k_y, \theta_0)/Q_l(k_y, \theta_0)$, which multiply the quasi-linear metric $\hat{\Lambda}(k_y, \theta_0)$ before integrating over θ_0 and k_y (see (3.7) and (3.8)). Figure 23 compares the nonlinear electron and main ion heat and particle fluxes computed from the nonlinear gyrokinetic database described in § 3 with

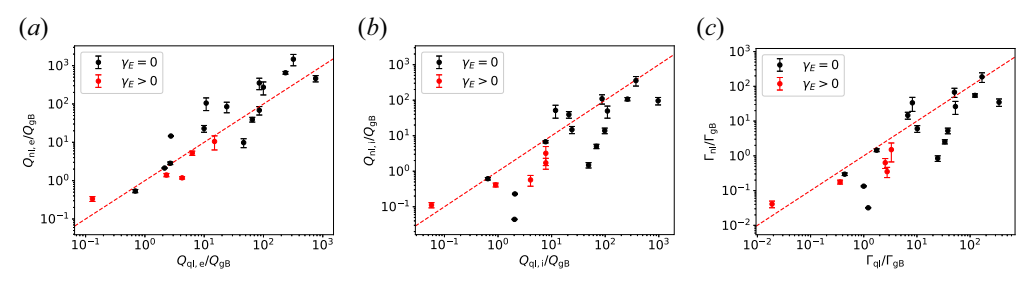


FIGURE 23. Comparison of the electron (a) and main ion (b) heat flux and total particle flux (c) computed from the nonlinear gyrokinetic database of § 3 with the quasi-linear heat and particle flux predictions given by (3.7) and (3.8).

the quasi-linear predictions given by (3.7) and (3.8). Parameters α and Q_0 have the values determined in the fit of the saturation model in (3.1) to the total heat flux from STEP nonlinear gyrokinetic simulations shown in figure 10.

An overall good agreement is observed between nonlinear and quasi-linear electron heat fluxes in figure 23(a), while the quasi-linear ion heat flux as well as the quasi-linear particle flux tend to overestimate the corresponding nonlinear quantities, as shown in figures 23(b) and 23(c). This is due to a slight overestimation of the quasi-linear weights $Q_{l,i}(k_y,\theta_0)/Q_l(k_y,\theta_0)$ and $\Gamma_l(k_y,\theta_0)/Q_l(k_y,\theta_0)$ with respect to nonlinear flux ratios, $Q_{nl,i}(k_y,\theta_0)/Q_{nl}(k_y,\theta_0)$ and $\Gamma_{nl}(k_y,\theta_0)/Q_{nl}(k_y,\theta_0)$. The agreement between the quasi-linear and the nonlinear ion heat flux (and the quasi-linear and the nonlinear particle flux) could be improved by introducing species-dependent coefficients, but this would further constrain the reduced model to the specific STEP regime of STEP-EC-HD.

REFERENCES

ANGIONI, C., GAMOT, T., TARDINI, G., FABLE, E., LUDA, T., BONANOMI, N., KIEFER, C.K., STAEBLER, G.M., ASDEX UPGRADE TEAM & EUROFUSION MST1 TEAM 2022 Confinement properties of L-mode plasmas in ASDEX Upgrade and full-radius predictions of the TGLF transport model. *Nucl. Fusion* 62 (6), 066015.

APPLEGATE, D.J., ROACH, C.M., COWLEY, S.C., DORLAND, W.D., JOINER, N., AKERS, R.J., CONWAY, N.J., FIELD, A.R., PATEL, A, VALOVIC, M., *et al.* 2004 Microstability in a "MAST-like" high confinement mode spherical tokamak equilibrium. *Phys. Plasmas* 11 (11), 5085–5094.

BARNES, M., ABEL, I.G., DORLAND, W., GÖRLER, T., HAMMETT, G.W. & JENKO, F. 2010 Direct multiscale coupling of a transport code to gyrokinetic turbulence codes. *Phys. Plasmas* 17 (5), 056109.

BARNES, M., DICKINSON, D., DORLAND, W., HILL, P.A., PARKER, J.T., ROACH, C.M., BIGGS-FOX, S., CHRISTEN, N., NUMATA, R., JASON, P., et al. 2022 GS2 v8.1.2, 10.5281/zenodo.6882296.

BELLI, E.A. & CANDY, J. 2008 Kinetic calculation of neoclassical transport including self-consistent electron and impurity dynamics. *Plasma Phys. Control. Fusion* **50** (9), 095010.

BOURDELLE, C., CITRIN, J., BAIOCCHI, B., CASATI, A., COTTIER, P., GARBET, X., IMBEAUX, F. & JET CONTRIBUTORS 2015 Core turbulent transport in tokamak plasmas: bridging theory and experiment with QuaLiKiz. *Plasma Phys. Control. Fusion* **58** (1), 014036.

CASATI, A., BOURDELLE, C., GARBET, X., IMBEAUX, F., CANDY, J. Clairet, F., Dif-Pradalier, G., Falchetto, G., Gerbaud, T., Grandgirard, V., et al. 2009 Validating a quasi-linear transport model versus nonlinear simulations. Nucl. Fusion 49 (8), 085012.

CASSON, F.J., PATTEN, H., BOURDELLE, C., BRETON, S., CITRIN, J., KOECHL, F., SERTOLI, M., ANGIONI, C., BARANOV, Y., BILATO, R., *et al.* 2020 Predictive multi-channel flux-driven modelling to optimise ICRH tungsten control and fusion performance in JET. *Nucl. Fusion* **60** (6), 066029.

- CITRIN, J., BOURDELLE, C., CASSON, F.J., ANGIONI, C., BONANOMI, N., CAMENEN, Y., GARBET, X., GARZOTTI, L., GÖRLER, T., GÜRCAN, O., *et al.* 2017 Tractable flux-driven temperature, density, and rotation profile evolution with the quasilinear gyrokinetic transport model QuaLiKiz. *Plasma Phys. Control. Fusion* **59** (12), 124005.
- CITRIN, J., TROCHIM, P., GOERLER, T., PFAU, D., VAN DE PLASSCHE, K.L. & JENKO, F. 2023 Fast transport simulations with higher-fidelity surrogate models for ITER. *Phys. Plasmas* **30** (6), 062501.
- CURIE, M.T., *et al.* 2022 A survey of pedestal magnetic fluctuations using gyrokinetics and a global reduced model for microtearing stability. *Phys. Plasmas* **29** (4), 042503.
- DI SIENA, A., NAVARRO, A.B., LUDA, T., MERLO, G., BERGMANN, M., LEPPIN, L., GÖRLER, T., PARKER, J.B., LODESTRO, L., DANNERT, T., et al. 2022 Global gyrokinetic simulations of ASDEX Upgrade up to the transport timescale with GENE–Tango. Nucl. Fusion 62 (10), 106025.
- DOERK, H., JENKO, F., PUESCHEL, M.J. & HATCH, D.R. 2011 Gyrokinetic microtearing turbulence. *Phys. Rev. Lett.* **106** (15), 155003.
- DORLAND, W., JENKO, F., KOTSCHENREUTHER, M. & ROGERS, B.N. 2000 Electron temperature gradient turbulence. *Phys. Rev. Lett.* **85** (26), 5579.
- DUDDING, H.G., CASSON, F.J., DICKINSON, D., PATEL, B.S., ROACH, C.M., BELLI, E.A. & STAEBLER, G.M. 2022 A new quasilinear saturation rule for tokamak turbulence with application to the isotope scaling of transport. *Nucl. Fusion* **62** (9), 096005.
- GIACOMIN, M., DICKINSON, D., KENNEDY, D., PATEL, B.S. & ROACH, C.M. 2023 Nonlinear microtearing modes in mast and their stochastic layer formation. *Plasma Phys. Control. Fusion* 65 (9), 095019.
- GIACOMIN, M., KENNEDY, D., CASSON, F., AJAY, C.J., DICKINSON, D., PATEL, B.S. & ROACH, C.M. 2024 On electromagnetic turbulence and transport in STEP. *Plasma Phys. Control. Fusion* 66 (9), 055010.
- GIACOMIN, M. & RICCI, P. 2020 Investigation of turbulent transport regimes in the tokamak edge by using two-fluid simulations. *J. Plasma Phys.* **86** (5), 905860502.
- GUTTENFELDER, W., CANDY, J., KAYE, S.M., NEVINS, W.M., WANG, E., BELL, R.E., HAMMETT, G.W., LEBLANC, B.P., MIKKELSEN, D.R. & YUH, H. 2011 Electromagnetic transport from microtearing mode turbulence. *Phys. Rev. Lett.* **106** (15), 155004.
- HAMED, M., PUESCHEL, M.J., CITRIN, J., MURAGLIA, M., GARBET, X. & CAMENEN, Y. 2023 On the impact of electric field fluctuations on microtearing turbulence. *Phys. Plasmas* **30** (4), 042303.
- HARDMAN, M.R., PARRA, F.I., PATEL, B.S., ROACH, C.M., RUIZ, J.R., BARNES, M., DICKINSON, D., DORLAND, W., PARISI, J.F., ST-ONGE, D., *et al.* 2023 New linear stability parameter to describe low-β electromagnetic microinstabilities driven by passing electrons in axisymmetric toroidal geometry. *Plasma Phys. Control. Fusion* **65** (4), 045011.
- HATCH, D.R., KOTSCHENREUTHER, M., MAHAJAN, S., VALANJU, P., JENKO, F., TOLD, D., GÖRLER, T. & SAARELMA, S. 2016 Microtearing turbulence limiting the JET-ILW pedestal. *Nucl. Fusion* **56** (10), 104003.
- HO, A., CITRIN, J., CHALLIS, C.D., BOURDELLE, C., CASSON, F.J., GARCIA, J., HOBIRK, J., KAPPATOU, A., KEELING, D.L., KING, D.B. 2023 Predictive JET current ramp-up modelling using QualiKiz-neural-network. *Nucl. Fusion* **63** (6), 066014.
- HORNSBY, W.A., GRAY, A., BUCHANAN, J., PATEL, B.S., KENNEDY, D., CASSON, F.J., ROACH, C.M., LYKKEGAARD, M.B., NGUYEN, H., PAPADIMAS, N., *et al.* 2024 Gaussian process regression models for the properties of micro-tearing modes in spherical tokamaks. *Phys. Plasmas* 31 (1), 012303.
- HOULBERG, W.A., SHAING, K.-C., HIRSHMAN, S.P. & ZARNSTORFF, M.C. 1997 Bootstrap current and neoclassical transport in tokamaks of arbitrary collisionality and aspect ratio. *Phys. Plasmas* **4** (9), 3230–3242.
- HUBA, J.D. 1998 NRL Plasma Formulary. Naval Research Laboratory.
- JENKO, F., DANNERT, T. & ANGIONI, C. 2005 Heat and particle transport in a tokamak: advances in nonlinear gyrokinetics. *Plasma Phys. Control. Fusion* **47** (12B), B195.
- JENKO, F., DORLAND, W., KOTSCHENREUTHER, M. & ROGERS, B.N. 2000 Electron temperature gradient driven turbulence. *Phys. Plasmas* **7** (5), 1904–1910.

- KENNEDY, D., GIACOMIN, M., CASSON, F.J., DICKINSON, D., HORNSBY, W.A., PATEL, B.S. & ROACH, C.M. 2023 Electromagnetic gyrokinetic instabilities in step. *Nucl. Fusion* **63** (12), 126061.
- KENNEDY, D., ROACH, C.M., GIACOMIN, M., IVANOV, P., ADKINS, T., SHEFFIELD, F., BOKSHI, A., DICKINSON, D., DUDDING, H.G., PATEL, B.S., *et al.* 2024 On the importance of parallel magnetic-field fluctuations for electromagnetic instabilities in STEP. Nucl. Fusion 64 (8), 086049.
- KINSEY, J.E., STAEBLER, G.M. & WALTZ, R.E. 2008 The first transport code simulations using the trapped gyro-Landau-fluid model. *Phys. Plasmas* 15 (5), 055908.
- KOTSCHENREUTHER, M., REWOLDT, G. & TANG, W.M. 1995 Comparison of initial value and eigenvalue codes for kinetic toroidal plasma instabilities. *Comput. Phys. Commun.* **88** (2–3), 128–140.
- KUMAR, N., CAMENEN, Y., BENKADDA, S., BOURDELLE, C., LOARTE, A., POLEVOI, A.R. & WIDMER, F. 2021 Turbulent transport driven by kinetic ballooning modes in the inner core of JET hybrid H-modes. *Nucl. Fusion* **61** (3), 036005.
- LUDA, T., ANGIONI, C., DUNNE, M.G., FABLE, E., KALLENBACH, A., BONANOMI, N., LUNT, T., SCHNEIDER, P.A., SICCINIO, M., TARDINI, G., *et al.* 2021 Validation of a full-plasma integrated modeling approach on ASDEX Upgrade. *Nucl. Fusion* **61** (12), 126048.
- MANDELL, N.R., DORLAND, W., ABEL, I., GAUR, R., KIM, P., MARTIN, M. & QIAN, T. 2024. GX: a GPU-native gyrokinetic turbulence code for tokamak and stellarator design, Journal of Plasma Physics 90 (4), 905900402.
- MARIANI, A., BRUNNER, S., DOMINSKI, J., MERLE, A., MERLO, G., SAUTER, O., GÖRLER, T., JENKO, F. & TOLD, D. 2018 Identifying microturbulence regimes in a TCV discharge making use of physical constraints on particle and heat fluxes. *Phys. Plasmas* 25 (1), 012313.
- MARIN, M., CITRIN, J., GARZOTTI, L., VALOVIC, M., BOURDELLE, C., CAMENEN, Y., CASSON, F.J., HO, A., KOECHL, F., MASLOV, M., *et al.* 2021 Multiple-isotope pellet cycles captured by turbulent transport modelling in the JET tokamak. *Nucl. Fusion* **61** (3), 036042.
- MEYER, H. FOR THE STEP PLASMA CONTROL AND HEATING AND CURRENT DRIVE TEAM AND CONTRIBUTORS 2022 The physics of the preferred plasma scenario for STEP. In *Proceedings of the 48th EPS Conference on Plasma Physics*.
- MITCHELL, J., PARROTT, A., CASSON, F.J., ERIKSSON, F.E., KOECHL, F., LENNHOLM, M., BARDSLEY, O., MEYER, H.F. & ALEIFERIS, S. 2023 Scenario trajectory optimization and control on step. *Fusion Engng Des.* **192**, 113777.
- NEVINS, W.M., WANG, E. & CANDY, J. 2011 Magnetic stochasticity in gyrokinetic simulations of plasma microturbulence. *Phys. Rev. Lett.* **106** (6), 065003.
- PATEL, B. 2021 Confinement physics for a steady state net electric burning spherical tokamak. PhD thesis, University of York.
- PATEL, B.S., et al. 2024 Pyrokinetics a Python library to standardise gyrokinetic analysis. J. Open Source Softw. 9 (95), 5866.
- PATEL, B.S., HARDMAN, M.R., KENNEDY, D., GIACOMIN, M., DICKINSON, D. & ROACH, C.M. 2023 $E \times B$ shear suppression of microtering based transport in spherical tokamaks. *Nucl. Fusion* (submitted).
- QIAN, T., BUCK, B., GAUR, R., MANDELL, N., KIM, P. & DORLAND, W. 2022 Stellarator profile predictions using Trinity3D and GX. *Bull. Am. Phys. Soc.*
- RAFIQ, T., WEILAND, J., KRITZ, A.H., LUO, L. & PANKIN, A.Y. 2016 Microtearing modes in tokamak discharges. *Phys. Plasmas* 23 (6), 062507.
- RICCI, P., ROGERS, B.N. & DORLAND, W. 2006 Small-scale turbulence in a closed-field-line geometry. *Phys. Rev. Lett.* **97** (24), 245001.
- RODRIGUEZ-FERNANDEZ, P., HOWARD, N.T. & CANDY, J. 2022 Nonlinear gyrokinetic predictions of SPARC burning plasma profiles enabled by surrogate modeling. *Nucl. Fusion* **62** (7), 076036.
- RODRIGUEZ-FERNANDEZ, P., WHITE, A.E., HOWARD, N.T., GRIERSON, B.A., ZENG, L., YUAN, X., STAEBLER, G.M., AUSTIN, M.E., ODSTRCIL, T., RHODES, T.L., *et al.* 2019 Predict-first experiments and modeling of perturbative cold pulses in the DIII-D tokamak. *Phys. Plasmas* **26** (6), 062503
- ROMANELLI, M., CORRIGAN, G., PARAIL, V., WIESEN, S., AMBROSINO, R., DA SILVA ARESTA BELO, P., GARZOTTI, L., HARTING, D., KOECHL, F., KOSKELA, T., et al. 2014 JINTRAC:

- a system of codes for integrated simulation of tokamak scenarios. *Plasma Fusion Res.* **9**, 3403023–3403023.
- STAEBLER, G.M., CANDY, J., HOWARD, N.T. & HOLLAND, C. 2016 The role of zonal flows in the saturation of multi-scale gyrokinetic turbulence. *Phys. Plasmas* 23 (6), 062518.
- STAEBLER, G.M., KINSEY, J.E. & WALTZ, R.E. 2005 Gyro-Landau fluid equations for trapped and passing particles. *Phys. Plasmas* 12 (10), 102508.
- STAEBLER, G.M., KINSEY, J.E. & WALTZ, R.E. 2007 A theory-based transport model with comprehensive physics. *Phys. Plasmas* 14 (5), 055909.
- STEPHENS, C.D., GARBET, X., CITRIN, J., BOURDELLE, C., VAN DE PLASSCHE, K.L. & JENKO, F. 2021 Quasilinear gyrokinetic theory: a derivation of Qualikiz. *J. Plasma Phys.* 87 (4), 905870409.
- SUGAMA, H., WATANABE, T.-H. & NUNAMI, M. 2009 Linearized model collision operators for multiple ion species plasmas and gyrokinetic entropy balance equations. *Phys. Plasmas* **16** (11), 112503.
- SUN, H., BALL, J., BRUNNER, S. & VOLČOKAS, A. 2024 A new quasilinear model for turbulent momentum transport in tokamaks with flow shear and plasma shaping. *Nucl. Fusion* **64** (3), 036026.
- THOLERUS, E., CASSON, F., MARSDEN, S.P., WILSON, T., BRUNETTI, D., FOX, P., FREETHY, S.J., HENDER, T.C., HENDERSON, S.S., HUDOBA, A., *et al.* 2024 Flat-top plasma operational space of the STEP power plant. Nucl. Fusion 64(10), 106030.
- WILSON, H., CHAPMAN, I., DENTON, T., MORRIS, W., PATEL, B., VOSS, G. & Waldon, C. 2020 STEP—on the pathway to fusion commercialization. In *Commercialising Fusion Energy: How Small Businesses are Transforming Big Science*, pp. 8–1. IOP Publishing.